Mutant huntingtin crosses the neuromuscular junction and causes transmission-selective pathological alterations in huntingtin expressing myotubes

Dinamarca C. Margarita[1,*], Colombo Laura[1,*], Brykczynska Urszula[1], Grimm Amandine[2], Tousiaki E. Natalia[1], Fruh Isabelle[3], Imtiaz Hossain[3], Gabriel Daniela[3], Eckert Anne[2], Müller Matthias[3] and Pecho-Vrieseling Eline[1]

1Neuronal Development and Degeneration Laboratory, Department of Biomedicine, University of Basel, Switzerland. [2]Neurobiology Laboratory for Brain Aging and Mental Health, Transfaculty Research Platform, Molecular & Cognitive Neuroscience, University of Basel, [3]Novartis Institute for Biomedical Research, Basel, Switzerland. [*]These authors contributed equally to this work.

Corresponding author: eline.pecho-vrieseling@unibas.ch

Abstract

Skeletal muscle dysfunction, wasting and synaptic pathology is a hallmark of Huntington's disease (HD). Similar as for the nervous system the pathological lesions and clinical symptoms progressively worsen with disease coarse. Cell-to-cell transmission of toxic mutant huntingtin (mHTT) has been shown to occur and could be a potential explanation for the progressive accumulation of pathological lesions and clinical symptoms in time. However, the mechanism and contribution of mHTT cell-to-cell transmission to pathology in an environment of ubiquitous expression of the mutant protein is not well understood. Here, we show that the HD-associated mHTT exon 1 (mHTTEx1) is transmitted from human induced pluripotent stem cell- (hiPSC-) derived motor neurons (MNs) to isogenic hiPSC-derived myotubes across functionally active neuromuscular junctions (NMJ) and *in vivo* in *wild-type* mice from the M1 motor cortex to spinal MNs and skeletal muscles. Increased synaptic connectivity and activity enhances transmission. Also, our data reveals that transmission happens prior to aggregate formation and that aggregation occurs progressively with continuous transmission across weeks at the myotube surface. Furthermore, we provide evidence that mHTTEx1 derived from MNs causes defragmentation of mitochondria and exacerbates nuclear aggregation, the latter in the presence of myotube autonomous mHTTEx1. Finally, we find that mHTTEx1 transmission results in decreased myotube contractions, in contrast myotube autonomous expression causes a hyperexcitable-like phenotype. Altogether, our data suggests that mHTTEx1 neuromuscular transmission contributes to skeletal muscle dysfunction in HD, via continuous transmission of the toxic protein already at early preclinical stages of HD and thereby contributes to an increasing accumulation of toxic protein in skeletal muscle, eventually leading to a highly-selective phenotype resulting in a decline of skeletal muscle function. Since multiple studies support a role of synaptic transmission of diverse misfolded proteins, including tau in Alzheimer's, α-synuclein in Parkinson's, mHTT in HD, tdp-43 in Amyotrophic lateral sclerosis and frontotemporal lobar dementia, in the central nervous system, this process likely represents a common synaptic-linked pathobiological pathway for most neurodegenerative protein misfolding diseases.

Introduction

Neurodegenerative protein misfolding diseases (PMDs) are a group of unrelated illnesses, including Alzheimer's-, Parkinson's-, Huntington's disease, Amyotrophic lateral sclerosis and frontotemporal lobar dementia. They are all characterized by misfolding and aggregation of a disease-specific protein, cell-type specific vulnerability to degeneration and progressive loss of structure and function of the nervous system. The disease process is already active for years, prior to revealing itself mostly around mid-age with initially discrete neurobehavioral and neuropsychiatric symptoms, which progressively worsen into cognitive impairment[1]. Currently no therapies are available to cure or at least slow down the progression of these devastating illnesses.

Recently, it has been suggested that cell-to-cell transmission of the toxic misfolded protein species might be a potential explanation for the spatiotemporal propagation of the pathological lesions through the brain. A casual-link between transcellular spreading of misfolded prion proteins (PrP scrapie or PrPSc) and pathology has been demonstrated in prion diseases[2]. For the other neurodegenerative PMDs it has been by now firmly demonstrated that tau (AD), α-synuclein (PD), mutant huntingtin (mHTT) and tdp-43 (ALS, FTLD) are transmitted between cells and functional connected brain regions in animal and cell culture models (for review see[3,4]). This transmission is accompanied by the appearance of protein aggregates in the acceptor cells and also a decline of cognitive and motor behavior has been observed in region- or cell-type specific misfolded protein-expression models of neurodegenerative PMDs [5-9].

Although the cellular mechanism responsible for cell-to-cell transmission of misfolded proteins has not been identified, it has been shown that synaptic connectivity and increasing neuronal activity enhances neuron-to-neuron transmission of Tau, and preventing synaptic vesicle release alters the neuron-to-neuron transmission of mHTT[10-13]. Together, with the observations that tau, α-synuclein, mHTT and tdp-43 are transmitted between functional connected brain regions *in vivo* in mice and drosophila, this strongly suggests a transsynaptic transmission pathway of misfolded proteins[5-8,10,12,14-16]. Synaptic connections are not only present in the CNS, but these structures also allow transcellular communication between the CNS and the periphery, as for example the neuromuscular junction (NMJ) between spinal motor neurons and skeletal muscles. mHTT expressed in either the skeletal muscle or brain in Caenorhabditis (C.) elegans have been shown to travel between the central nervous system and skeletal muscles[17]. Thus, transmission of misfolded proteins could represent a systemic disease pathway affecting not only the CNS, but also contributing to a progressive deterioration of peripheral systems.

Patients with HD suffer from a decline in skeletal muscle function, which progressively worsen with disease course[18,19]. HD is an autosomal dominant disorder that develops with hundred percent penetrance when the number of CAG triplets in the HTT gene exceeds 35 repeats. This is translated into a pathogenic polyglutamine stretch in the exon1 of the protein[20]. Incomplete mRNA splicing of the mHTT results in the very toxic exon 1 fragment of the protein, which is highly prone to aggregation and it aberrantly translocates to the nucleus where it interferes with transcription[21-23]. Human neuronal cell lines expressing only the HTT exon 1 (HTTEx1) develop intra-nuclear inclusions and mitochondrial dysfunction[24]. These pathologies are also observed in skeletal muscles of HD patients and animal models, together with skeletal muscle wasting and fatigue[19,25-30].

Using an isogenic human induced pluripotent stem cell- (hiPSC-) neuromuscular (NM) model combined with high-throughput live-cell imaging, functional analysis and microfluidic systems, we addressed whether mHTTEx1 cell-to-cell transmission can occur across the neuromuscular junction and how synaptic activity and density could influence this process. We

also examined whether mHTT NMJ transmission can contribute to skeletal muscle pathology including conditions resembling ubiquitous expression of mHTTEx1. We show that mHTTEx1 is transmitted from neurons to myotubes across the NMJ and that transmission is elevated by increased NMJ density and enhanced activity. Moreover, our data reveal that transmission occurs independent of mHTTEx1 aggregation, already during NMJs assembly and is enhanced during their functional maturation. Furthermore, our data discloses that mHTTEx1 transmission results in fragmented mitochondria, a functional decline of the NMJ and increased intra-nuclear aggregates in the presence of cell autonomous mHTTEx1 in myotubes. Finally, we show that mHTTEx1 transmission expressed specifically in the pyramidal neurons in the M1 motor cortex *in vivo* in mice is transmitted to the spinal motor neurons and triceps and biceps muscles. Our findings therefore suggest that mHTTEx1 cell-to-cell transmission occurs between the central nervous system and the periphery and might contribute to pathological alterations of the NM system already at early, preclinical stages of the disease. More broadly, our findings also support the notion that cell-type specific vulnerability might be determined by the level of functional synaptic connectivity in combination with transsynaptic transmission of the misfolded proteins.

Results

Characterization of an *in vitro* neuromuscular co-culture using hiPSC-derived neuronal and muscle cell lines to study the mechanisms and pathological consequences of trans-neuromuscular transmission of pathogenic HTT. To assess whether mHTT transmission can contribute to skeletal muscle pathology in HD patients, we designed an *in vitro*, isogenic hiPSC-derived neuromuscular co-culture system, using two transgenic cell lines, one bearing a doxycycline- (dox)-inducible pro-neuronal transcription factor, *neurogenin 2* (*Ngn2*) transgene[31] and a second one bearing a Dox-inducible pro-skeletal muscle transcription factor, *myoblast determination protein 1* (*MyoD*) transgene. We generated four isogenic hiPSC *Ngn2* and one hiPSC *iMyoD* line, isogenic to the *Ngn2* lines, to establish the following two NM-co-culture systems: **1)** a *Ngn2* line expressing the *exon1* of the HTT gene, with 72 (pathogenic) triplets encoding for glutamine, fused to a *Cre* sequence without the additional nuclear localization signal (*iNgn2;HTTEx1Q72-Cre*) and a MyoD hiPSC line with a LoxP-GFP construct (*iMyoD;LoxP-GFP*; Supplemental Fig. 1a). The Cre-Lox system allows us to follow HTTEx1Q72-Cre transmission to LoxP-GFP myotubes by myotubes turning green and can be used for high-throughput, low-resolution, live-cell imaging to follow transmission and NM-activity in the same culture over weeks (Fig. 1a); **2)** a HTTEx1Q72 fused to a mCherry (*iNgn2;HTTEx1Q72-mCherry;* Supplemental Fig. 1a). The mCherry-tag allows to follow more precisely the HTTEx1Q72 transmission to myotubes over time at protein level. Once a LoxP-GFP myotube is expressing GFP, further transmission of HTTEx1Q72 cannot be visualized. In contrast, a change in mCherry labelling will reveal the dynamics of this process and it will allow to correlate the amount of transmitted protein with pathology. Importantly, comparing the transmission of HTTEx1Q72 fused to different tags serves as a control to determine that transmission is independent of the tag.

Successful expression of the HTTEx1Q72-Cre and HTTEx1Q72-mCherry constructs in iPSCs was determined by western blot (WB) analysis using an antibody against HTT exon 1 (MAB5492) (Supplemental Fig. 1b). Comparing the expression levels between the lines revealed that we had clones with different levels of HTTEx1Q72-mCherry expression (Band intensity HTTEx1Q72 / β-actin = clone#71 0.26, clone#72 0.22 and clone#75 1.53). The HTTEx1Q72-Cre

line expressed the lowest compared to HTTEx1Q72-mCherry clones because to visualize the band on the gel we had to expose the gel much longer (Supplemental Fig. 1b). To assess whether the different protein expression levels result in distinct propensity to aggregation we differentiated the hiPSC lines into neurons. After day of co-culture (DCC) 1 we observed a decrease in Oct4 expression, meaning that the cells are losing pluripotency as expected (Supplemental Fig. 1c). The neurons were labelled after 7 and 21 days of differentiation with the HTT-specific antibody, Em48 which has high affinity for the aggregated form. This revealed that aggregation increased with increasing expression level of the HTTEx1Q72 protein, with HTTEx1Q72-Cre showing the lowest and clone#75 HTTEx1Q72-mCherry the highest Em48 values in the neurons (Supplemental Fig. 1d).

To test the cre-lox system, we electroporated *iMyoD;LoxP-GFP* iPSCs with the *HTTEx1-Cre* construct and the *iNgn2;*HTTEx1Q72-Cre iPCSs with a *LoxPP-mCherry* plasmid. This resulted in GFP and mCherry expressing cells, resp. In the absence of Cre we never observed GFP expression in the *iMyoD;LoxP-GFP* hiPSCs (n = 3; Supplemental Fig. 1e). Altogether, these analyses demonstrate a successful generation of four hiPSC-lines, which can be used to study cell-to-cell transmission of HTT by the appearance of either GFP positive myotubes or mCherry+ aggregates in myotubes.

Formation of functional neuromuscular junctions in co-cultures of Q72-Cre neurons with LoxP-GFP myotubes.

In the next step we established from these new lines NM-co-cultures using a two-step differentiation protocol (Supplemental Fig. 2a). To induce differentiation into either neurons or myoblasts (myocyte precursors) the hiPSCs were exposed for 3-days to dox. After these 3 days the myoblasts were seeded and cultured for additional 10 days in myotube (fused myocytes) promoting media. The precursor neurons were seeded directly after the 3-day dox treatment on top of the myotubes and the culture medium was changed to a motor neuron promoting type (Supplemental Fig. 2a). Maturation of the myotubes and neurons in co-cultures was assessed by WB at DCC 1, 7, 14, 21 and 28, using myotube-specific antibodies (myotube heavy chain embryonic and postnatal isoform (MHC3 and MHC8, resp.) and neuronal (doublecortin (DC; neuronal precursor marker) and motor neuron, specific antibodies (Islet 1 and choline acetyl transferase (ChAT)) (Fig. 1b). In co-cultures protein levels of MHC3 decreased and MHC8 increased from DCC 1 to 28. DC decreased and ChAT increased from DCC 7-28. This demonstrates a molecular maturation of the two cell types, hereafter referred to as Neu Q72-Cre for the neurons and Myo LoxP-GFP for the myotubes. To assess whether NMJs are formed between Neu Q72-Cre and Myo LoxP-GFP, we performed immunofluorescence antibody staining (IF) on the co-cultures and observed close appositions of the neuronal presynaptic active zone marker bassoon and the acetylcholine receptor (AChR) marker α-bungarotoxin (α-BgTx) on myotubes (which represent the postsynaptic structure of the NMJ; Fig. 1c). Patch-clamp recordings from Neu Q72-Cre revealed functional maturation of a current-induced action potential firing pattern from a mixed phasic / adaptive at DCC7 to a mainly tonic pattern at DCC 21 (Fig. 1d, Supplemental Fig. 2b). To assess whether these neurons can induce myotube contractions, we performed live-cell imaging of the co-cultures and visualized myotube contractions at DCC 15 (movie 1). To reveal that these contractions are induced by neuronal activity we recorded these

contractions at DCC 21 in the absence and presence of the NMJ-activity blocker α-BgTx. Myotube contractions were present in the absence of α-BgTx (% total contracting area / well area = 0.35± 0.099, mean ± s.e.m.) and disappeared upon its addition to the co-culture (0.047 ± 0.018, mean ± s.e.m.). These data demonstrate the establishment of functional NMJs between Neu Q72-Cre and Myo LoxP-GFP. To gain better insight into the temporal development of these NMJs we followed myotube contractions for 29 days. Recordings were performed from the same wells and analyzed for "total myotube activity" and "total myotube contracting area". We compared co-cultures with monocultures of Myo LoxP-GFP. This revealed a temporal increase in both myotube activity and contracting area only in co-cultures (Fig. 1e). In addition, we analyzed the variability of these parameters within one culture well. The variability significantly decreased from DCC 15 onwards in co-cultures, but stayed high in monocultures (Supplemental Fig. 2c). Spontaneous myotube contractions occur randomly, while neuron-induced contractions are triggered. Interestingly, the decrease in variability occurs at a time point when the myotube contracting area steeply increases (DCC 15 to 22, $p = 0.004$), and in parallel with the maturation of neuronal properties allowing a more active AP firing pattern establishment (DCC 14 to 21, tonic firing from 14% to 80%) (Fig. 1d, e). These data together demonstrate the establishment of functional NMJs between Neu Q72-Cre and Myo LoxP-GFP in this NM-co-culture system and validates it for addressing the question whether HTTEx1Q72-Cre can be transmitted from motor neurons to myotubes across functional NMJs.

Trans-NM transmission of HTTEx1Q72-Cre occurs with time and in the absence of aggregates in the neurons.

Next to assessing myotube contractions, we performed high-throughput live-cell fluorescent imaging from the same wells from DCC 4 to 28. At DCC 4 first GFP+ myotubes appeared and their number increased with co-culture time until day 14, after that the number stayed stable (Fig. 1f, g) (DCC4 2.94±0.42; DCC7 10.50±1.27; DCC14 21.18±1.80; DCC21 24.27±3.35; DCC28 24.81±1.94; mean ± s.e.m). Based on Em48 staining at DCC 7 and 21 (Supplemental Fig. 1d) we did not observe aggregated form of HTT in HTTEx1Q72-Cre neurons. When we stained the co-culture at DDC 28 we detected presence of Em48 positive aggregates selectively in GFP+ myotubes (Fig. 1h). Transmission thus likely occurs in a non-aggregated form and aggregation takes place in the myotubes.

To prove that Q72-Cre NM transmission requires direct cell-cell contact and is not transferred via the culture media, we placed a two-chambers cell culture insert w/o bottom in one dish to allow physical separation of Neu Q72-Cre from Myo LoxP-GFP, while the medium was shared. The dish surface surrounded by one chambers was coated with Poly-L-lysine and laminin to support neuronal attachment and here Neu Q72-Cre were seeded. The surface delimited by the second chamber was coated only with laminin to support myotube attachment and here myotubes were seeded. The surface between the inserts was not coated to prevent the movement of the cells and extension of the axons to the myotubes. At DCC 1 the inserts were removed and the cultures were screened for GFP+ myotubes until 21 DCC (Supplemental Fig. 3a). In these co-cultures we never observed GFP+ myotubes (Supplemental Fig. 3b).

Taken together, the NM-co-culture system allows to follow pathogenic HTTEx1 cell-to-cell transmission over weeks with high-throughput low-resolution live-cell imaging. This is important, because transmission of misfolded proteins is likely a continuous process. Furthermore, with the

expression of GFP in Myo LoxP-GFP we demonstrated that transmitted HTTEx1Q72-Cre can enter the cytosol and the nucleus. Finally, the low number of aggregates present in GFP+ myotubes strongly suggests that spreading occurs prior to aggregate formation.

NM-co-cultures in microfluidic devices reveal HTTEx1Q72 transmission across the NMJs. To further demonstrate that HTTEx1Q72 is transmitted across the NMJ and assess whether these structures play a role in determining the efficiency of pathogenic HTT transmission we established NM-co-cultures in microfluidic devices (MFDs). These devices allow to co-culture two cell populations in two fluidic isolated compartments. The compartments are connected with microgrooves of 450 µm length, through which axons can grow and reach the other compartment (Fig. 2a, upper panel). This setup assures that the only contact between neurons and myotubes can be via the presynaptic side of the axons, which terminate on the myotubes to form the NMJ. To study the efficiency of HTTEx1Q72 NM transmission we used here the Neu Q72-mCherry clone#75. We first assessed whether NMJs are formed between Neu Q72-mCherry and Myo LoxP-GFP (we kept using this myotube line, but to prevent confusion in this article we will refer to it as Myo when we describe the experiments performed in co-culture with Neu Q72-mCherry). The mCherry labeling of the Q72-mCherry expressing neurons showed that these projected their axons from the presynaptic neuronal compartment to the postsynaptic myotube compartment (Fig. 2a, lower panel). In the myotube compartment NMJs were established, as visualized with IF staining's of Bassoon and AChR appositions at DCC21 (Fig. 2b). In a study by Lutz et al., 2020[32] it has been shown that the AChR clusters, labelled with α-BgTx, on the surface of myotubes can be classified based on their shapes. We performed a detailed shape anaylsis of these clusters at DCC21 and detected four different types in our cultures, which we classified as small&elongated, small&round, big&elongated, big&round (Supplemetal Fig. 4a-c). When we compared the clusters of mono Myo with co-cultures of Neu Q72-mCherry and Myo we found that even though the small&round cluster type are the majority in both cultures, there was a significant increase in the density of both types of big clusters in the co-cultures compared to the mono Myo cultures (Supplemental Fig. 4d,e). The big-cluster types are thus likely those constituting the NMJs. Supporting this notion, we found that big cluster types were over-represented among those associated with the presynaptic marker Bassoon, compared to the clusters w/o Bassoon (Fig. 2c). With these analyses we demonstrate the presence of structural NMJs in the co-cultures grown in MFDs. To judge whether Neu Q72-mCherry clone#75 neurons are able to potentially trigger myotube contractions we performed patch-clamp recordings and found that these cells develop from DCC 7 to 21 a more active pattern of current-induced action potential firing pattern from mainly phasic at DCC 7 to mainly adaptive at DCC 21 (Fig. 2d).

Next we assessed whether Q72-mCherry protein is present in the myotubes in the postsynaptic compartment. IF labeling of the myotubes indeed revealed transmission of Q72-mCherry from the neurons in the presynaptic compartment to the myotubes (Fig. 2e). Similar as for the Q72-Cre and Myo LoxP-GFP co-cultures, we found that the transmission of Q72-mCherry to Myo across the NMJ occurs over time. In contrast to reaching a plateau at DCC 21 that we observed for Neu Q72-Cre, for the Neu Q72-mCherry we revealed a continuous increase from DCC 7 to DCC 28 of Q72-mCherry aggregates in the myotubes, with the steepest increase occurring between DCC 15 and 21 (Fig. 2f; DCC7 1±0.2; DCC15 15±3; DCC21 78±12; DCC28 124±15; mean ± s.e.m.; n=45 images for each time point). We analyzed the volume of Q72-

mCherry aggregates over time and found that with co-culture time there developed a distribution in size, which we divided in four groups (size in μm^3: ≤ 1, > 1 ≤ 5, > 5 ≤ 10, > 10; Fig. 2g). From DCC 14 to 21 there was a large increase in the number of aggregates of ≤ 1 µm (DCC 14: 77 and DCC21: 2921). Together with this, the amount of bigger aggregates also increased with time (DCC 14 vs DCC21: > 1 ≤ 5: 47 vs 534, > 5 ≤ 10: 15 vs 66, > 10: 6 vs 25), suggesting both arrival of new small aggregates and aggregation of protein to form bigger size aggregates. Thus, we could show that spreading occurs i) when the axons provide the only possible connection between neuronal and muscle cells and ii) regardless of the tag fused to the exon1.

The load of Q72-mCherry aggregates correlates to increasing neuromuscular connections.
A pathology already present at presymptomatic stages in HD patients is a loss of functional neuronal connectivity in white matter pathways. This pathology arises first in the cortico-striatal pathway and then progresses to cortical and other subcortical brain regions[33-37]. Interestingly, the most vulnerable brain regions are so called 'rich club', this are brain regions which are more highly connected to each other, forming a selective network with higher connectivity than other brain regions[38]. These are brain nuclei which receive a particularly high number of synaptic connections. It has been suggested that transsynaptic neuron-to-neuron transmission of mHTT could be a potential underlying pathobiological mechanism for the early loss of synaptic connections[35]. To assess whether a higher density of NMJ connections leads to more Q72-mCherry aggregates in myotubes, we divided the postsynaptic myotube compartment into 3 bins. Bin 1 was closest to the microgrooves and Bin 3 furthest away. The Axonal area normalized to the myotube area was highest in bin 1 and decreased from bin 1 to 3 (in μm^2: Bin 1 0.079±0.008; Bin 2 0.029±0.004; Bin 3 0.013±0.003; mean ± s.e.m.; n=15 images; Fig. 3a, b). We further found that the number of Q72-mCherry aggregates in myotubes at DCC21 was highest in bin 1 and steeply decreased from bin 1 to 3 (in μm^2: Bin 1 155.6±22.93; Bin 2 70.33±8.31; Bin 3 8.067±1.42; mean ± s.e.m.; n=15 images; Fig. 3a, c). Interestingly, when we quantified the number of aggregates from DCC7 to 28 we observed a similar, but delayed increase in the number of aggregates in bin 2 compared to bin 1 (Supplemental Fig 5a). Axons will arrive slightly later in bin 2 than bin 1 and thus the formation of NMJ is expected to be slightly delayed in bin 2 compared to bin 1, which likely explains this temporal delay in Q72-mCherry aggregates accumulation in myotubes. Although minor transmission occurred to bin 3, the temporal pattern was similar to bin 1 and 2, with the highest number of Q72-mCherry aggregates at DCC 28 (Supplemental Fig 5a). Since we assumed that Q72-mCherry proteins reach the myotubes via the NMJs, we next compared the number of Q72-mCherry aggregates in myotubes to the density of NMJs. We found a positive correlation between the density of NMJs and the number Q72-mCherry aggregates in myotubes (Fig. 3d, e). Thus, these analysis reveal that a higher density of NM-connectivity results in more Q72-mCherry aggregates in myotubes and thus strongly suggest a trans-NMJ path of transmission.

Q72-mCherry aggregates mainly associate with big AChR clusters.
Previously we showed that mHTT is transmitted from mouse cells to human stem cell-derived neurons (h-neurons) in co-cultures of HD-derived mouse organotypic brain slices (OTBS) with h-

neurons. In this system transmission occurred mainly between week 2 and 4 of co-culture. During this time period mHTT co-localized with the pre- and postsynaptic markers synaptophysin and post-synaptic density protein-95 (PSD-95) in neurons, resp.[12]. In the NM-co-cultures we also observed around 25% of Q72-mCherry aggregates to be associated with the postsynaptic AChRs (Supplemental Fig. 4b). Interestingly, around 70% of the AChR cluster types associated with Q72-mCherry aggregates were of the big-type, while among those w/o Q72-mCherry aggregates only around 12 % were big (Fig. 3f). The big clusters are likely representing those incorporated in the NMJ, since this type increased in the presence of neurons and also in association with the presynaptic marker Bassoon (Supplemental Fig. 4e, Fig. 2 c). Since we observed much higher increase in Q72-mCherry transmission between DCC 15 and 21 (30 fold) comparing to DCC 7 and 15 (10 fold) (Fig. 2f) we propose that Q72-mCherry is transmitted most efficiently via established NMJs.

Increasing neuronal activity results in higher NM transmission of Q72-mCherry.

Neuron-to-neuron transmission of mHTT in the OTBS – h-neuron co-cultures and also *in vivo* in drosophila has been shown to be vastly blocked by preventing SNARE-dependent fusion of synaptic vesicles to the presynaptic membrane[10,12]. This impairs release of synaptic vesicles content from the presynaptic membrane. On the contrary, depolarization of neurons results in increased AP firing which triggers synaptic vesicle release[39]. To test whether an increase in neuronal activity effects Q72-mCherry NM transmission, we depolarized the Neu Q72-mCherry Clone#72 by exposing them for 10 minutes to an artificial cerebrospinal fluid (ACSF) solution with high KCl concentration (10mM) and kept them after this acute treatment for 2 hours in ACSF with 2.5mM KCl (Fig. 4a). We chose to use the clone#72 for this experiment, because of its lower expression of Q72-mCherry, which makes it a more appropriate line to detect changes in transmission upon manipulations. The exposure to 10mM KCl resulted in more Q72-mCherry aggregates in myotubes compared to those co-cultures which were exposed to 2.5mM KCl (67±10 with KCl 10mM, compared to 37±6 with 2.5mM KCl, n=12 images) (Fig. 4b, c). The volume of Q72-mCherry puncta in myotubes was slightly smaller after KCl treatment (ctr = 0.69 ± 0.11 μm^3, KCl = 0.57 ± 0.10 μm^3; Fig. 4d) and significantly more puncta were found deeper inside the myotubes (measured as a distance from the MHC1 surface created by Imaris; ctr = -0.20 ± 0.03 and KCl 10 mM = -0.051 ± 0.03 µm from the surface, p = 0.0001) (Fig. 4e). This may indicate a more active internalization and distribution of the aggregates in myotubes during increased trans-synaptic activity.

Q72-mCherry aggregates accumulates at the myosin surface.

Our results so far demonstrate a trans-NM pathway of HTTEx1Q72 transmission. To reveal a potential pathology which the transmitted HTTEx1Q72 can cause, we first assessed the intracellular localization of this protein in the myotubes in co-culture with Neu Q72-mCherry clone#75, from DCC 7 to 28. In particular, we analyzed the localization of the Q72-mCherry aggregates at the cellular surface. We used the surface function of the Imaris software (Oxford Instruments) to define the surface of myotubes based on MHC1 staining. By visual inspection of images, we observed a striking localization of the aggregates to and partially passing through the MHC1+ myotube surface (Fig. 5a, b). Based on a quantification, at DCC 7 the Q72-mCherry aggregates both localized at the myotube surface (at the surface = within 0 – 0.05 µm from the

myotube surface) and inside the myotube (inside = > 0.05 µm away from the myotube surface) and were mostly small (majority below 4 μm^3) (Fig. 5c, d). At DCC 15 more Q72-mCherry aggregates accumulated at the surface compared to inside, from DCC 21 this gradually shifted to more aggregates inside the myotubes (Fig. 5c, d). Furthermore, as we found before, Q72-mCherry aggregates with larger volume were observed with increasing co-culture time and growing number of Q72-mCherry aggregates (Fig. 5c). It has been shown that mHTT has high affinity for bioengineered lipid membranes and that insertion of these proteins into these membranes triggers their aggregation (Marquette, A. and Bechinger, B. bioRxiv 2020). Our analysis also revealed that the largest Q72-mCherry aggregates were localized at the myotube surface (Fig. 5c). Indeed, when we selectively looked at the localization of aggregates with a volume larger than 5 μm^3, we found that at DCC 7 and 28, 50 and 48% resp. and at DCC 15 and 21, 95 and 93% resp. were at the myotube surface (Fig. 5e).

Neuronal expression of Q72-mCherry induces and aggreviates pathological alterations in myotubes.

An important open question in the field of misfolded protein transmission is whether the transmitted pathology can aggravate the pathology caused by the cell-autonomous presence of the toxic protein. This question is crucial to address, because it will reveal whether toxic protein transmission is an important novel disease pathway in neurodegenerative PMDs. Therefore, we assessed HD-specific pathological alterations in myotubes in the following Neu Myo co-culture combinations: 1) Neu control (ctr)/Myo ctr (Myo ctr are the Myo LoxP-GFP used throughout this publication. For clarity we refer here to this line as ctr. Control means no expression of the pathogenic HTTEx1Q72), 2) Neu ctr/Myo Q72-mCherry (cell-autonomous), 3) Neu Q72-mCherry/Myo ctr (transmission) and 4) Neu Q72-mCherry/Myo Q72-mCherry (transmission + cell autonomous).

Mitochondrial dysfunction is a characteristic observed in skeletal muscle obtained from HD patients and animal models[19]. Typically a disbalance in the fission and fusion events occur which lead to more fragmented structures and a reduced filamentous network[28,40]. To assess the effect of cell-autonomous and transmitted HTTEx1Q72 on structural aspects of mitochondria we analyzed mitochondrial length, area weighted form factor and form factor in control co-cultures and compared these parameters with those measured in cell-autonomous and transmission co-cultures. We used MFDs to avoid contamination with mitochondria coming from the neurons. In this particular experiment we did not analyze cell autonomous + transmission co-cultures, because the expression of the mCherry reporter in both cell types would not allow us to discriminate between myotubes which received Q72-mCherry from neurons from those which did not. We observed a significant reduction in all three parameters when HTTEx1Q72-mCherry was expressed in myotubes and when the myotubes received HTTEx1Q72-mCherry from the neurons (clone#75) (Fig. 6a). A fragmentation of the mitochondrial filamentous network due to altered structural mitochondrial dynamics is very likely to impair mitochondrial and cellular function. For example, in HD patient skeletal muscles a reduction in ATP production has been observed and patients suffer from exercise-induced muscle fatigue already at preclinical stages of the disease[27,29]. Therefore, we assessed whether the presence of HTTEx1Q72 has also an effect on myotube contraction. We recorded the contraction activity and area of myotubes in the different mixed-genotype co-cultures and observed a larger myotube contraction activity and area in cell

autonomous compared to control co-cultures at DCC 15 and 22 (Fig 6b). When HTTEx1Q72 (clone#75, high expression) was present in neurons, either in transmission or in transmission + cell autonomous co-cultures there was a complete loss of myotube contractions, despite the fact that these neurons displayed AP firing upon current injections (Fig. 6b, 2d). In transmission co-cultures with Neu Q72-cre (low expression) the contraction parameters were not different from control cultures, but in transmission + cell autonomous co-cultures the activity was significantly increased at DCC 15 and 22 compared to control, but not anymore at DCC29 (Fig. 6b). The contracting area was only significantly increased at DCC15 compared to control (Fig. 6b). The contracting parameters were significantly larger in transmission + cell autonomous compared to transmission co-cultures from DCC 15 onwards (Fig. 6b). Interestingly, compared to cell autonomous expression alone, cultures which had transmission always had significantly lower contraction parameters from DCC 15 and these difference increased with higher expression of Q72 (compare line Neu Q72-cre with Q72-mCherry). There was no difference in contraction parameters between monocultures of Myo Q72-mCherry (Cre) and Myo Ctr (data not shown). Thus, neuromuscular communication is weakened by expression of HTTEx1Q72 in neurons in an dose dependent manner, but not when its expression is restricted to myotubes. In contrast, expression of HTTEx1Q72 in myotubes alone results in increased myotube contraction activity and area compared to ctr cultures.

We decided to have a closer look at the myotubes and analyzed the extend of nuclear accumulation of HTTEx1Q72-mCherry aggregates. An increase of nuclear aggregates correlates with a worsening of skeletal muscle pathology in the R6/2 mouse models of HD[30]. Moreover, previously we showed that mHTTEx1 transmitted from mouse cells to human stem cell-derived neurons, first appeared as cytoplasmic aggregates and with time aggregates appeared in the nucleus. Nuclear aggregation correlated with the time when pathological changes occurred in the human neurons[12]. In the co-cultures of mixed genotypes, we observed the lowest number of nuclear aggregates in transmission co-cultures (4.59±0.9; mean ± s.e.m.), this number slightly increased when the protein was expressed cell autonomously in myotubes (9.17±0.94; mean ± s.e.m.) and significantly increased in the concurrent presence of cell autonomous expression and transmission from neurons (19.9±2.32; mean ± s.e.m.) (Fig. 6c).

Mutant HTTEx1 is transmitted from the motor cortex to skeletal muscle *in vivo* in mice

With the *in vitro* experiments we so far demonstrated that mutant HTTEx1 is transmitted across the NMJ from neurons to muscle cells and that this induces pathological changes in the receiving myotubes. To understand whether this phenomenon is also likely to occur in patients we studied the transmission of mutant HTTEx1 from the motor cortex to the skeletal muscles *in vivo* in mice. To this end we designed adeno-associated viruses carrying a LoxPPed HTTEx1Q138-v5 plasmid (AAV_LoxP-Q138-v5). We chose a longer (138) CAG repeat, since mice are more resistant to CAG repeat expansion than humans. In order to further confirm that the longer mCherry and Cre reporter tags that we used in *in-vitro* experiments are not the driving force of the mutant HTTEx1 cell-to-cell transmission, we used in this experiment a 9 amino acid long v5 reporter tag. The AAV_LoxP-Q138-v5 was injected in the motor cortex M1 of mice expressing cre selectively in pyramidal neurons (nex-cre mice). We observed Q138-v5 expression in the motor cortex (Fig. 7a). After 6 Months we analyzed the brachial spinal cord and the Triceps and Biceps forelimb

muscles and found Q138-v5 positive aggregates in spinal motor neurons and both muscles (Fig. 7b, c).

In skeletal muscle of healthy human subjects mHTT mRNA is detected, but no HTT protein[41]. We performed WB analysis from *wild-type* mouse whole brain, cortex and skeletal muscle tissue and used an antibody against the full-length (fl) endogenous protein (MAB2166). We found fl-HTT in both whole brain and cortex samples, but not in samples from skeletal muscles (Fig. 7d).

Discussion

Despite the genetically unrelated cause of the different PMDs, they show some striking commonalities, which strongly suggests a common underlying pathobiological mechanism. In all of these disorders the disease-associated proteins transmit through the brain similarly as the propagation of pathological lesions[3,42]. The brain regions with highest connectivity are most vulnerable and the loss of functional connectivity occurs prior to neurodegeneration[43-45]. Whether cell-to-cell transmission of mHTTEx1 is regulated by functional synaptic connectivity and can contribute to disease in an environment of ubiquitous expression of the mutant protein is to date not well understood. Here, we established an *in-vitro* hiPSC derived neuro-muscular co-culture system to study the role of neuromuscular connections in the development of HD-related skeletal muscle pathology. We provide evidence that trans-neuromuscular transmission of mHTTEx1 can occur across the neuromuscular synapse, likely already at early preclinical stages of disease, and contributes to skeletal muscle pathology. Furthermore, our findings suggest that mHTTEx1 transmission is more efficient when synaptic activity and density are increased. Finally, we show that mHTTEx1 is transmitted along the corticospinal pathway to skeletal muscles *in vivo* in mice.

N-terminal mHTTEx1 transmission across the neuromuscular synapse

In our study, we evaluated the transmission of N-terminal mHTTEx1 through the NMJ.

As we previously showed, the protein is transmitted in co-cultures of HD organotypical brain slices with healthy hSC-derived neurons starting at a time point coinciding with the establishment of functional synapses and is being enhanced in the following weeks[12]. Similarly, in our current study we show that transmission of HTTEx1Q72-Cre, visualized by the appearance of GFP+ myotubes (Myo LoxP-GFP) mainly occurs at a time point when functional NMJs are established. We further confirmed this data in the MFD system which restricts the neuron and muscle contact to the axonal connections. In order to visualize morphological establishment of NMJ in this system we performed an in-depth analysis of the AChR clusters (post-synaptic muscular part of NMJ) on the myotubes. AChRs are found diffused throughout the myotubes and are organized into complex clusters in the progress of development, leading to a formation of platforms for NMJ formation[32,46]. Those clusters that were in close contact with bassoon (pre-synaptic neuronal protein of NMJ) were in majority of large and round or large and elongated types, in contrast to small clusters that represent the diffused AChRs. The large clusters were also those that increased in number upon addition of neurons to the muscular cultures, strongly suggesting they represent functional NMJs. These are the AChR clusters that we also found more frequently associated with HTTEx1Q72-mCherry aggregates. Patch-clamp recordings from Neu Q72-mCherry in these cultures showed

that neurons have reached a higher frequency of action potential firing at the time point when transmission peaked (DCC21). Thus, both experimental systems support that mHTTEx1 is transmitted across functional established NMJs. These *in-vitro* findings we could validate *in-vivo* in mice by showing that HTTEX1Q138-v5 was transmitted from the M1 motor cortex to spinal motor neurons and to the triceps and biceps muscles. Similar, kim et. al., expressed non-pathogenic (Q25) and pathogenic (Q97) HTTEx1 in both neurons and muscles of the pharyngeal system in C. elegans and found that cell-to-cell transmission occurred bidirectional, with significantly higher efficiency for Q97 compared to Q25[17].

In line with a transsynaptic pathway of mHTTEx1 transmission, our work provides evidence that synaptic density and activity regulate cell-to-cell transmission of mHTTEx1. First, we showed that in the region of the MFD with highest number of axonal projections there were more Q72-mCherry aggregates found in muscle cells than in regions with less axonal projections. Furthermore, we quantified the density of Bassoon and AChR associations (morphological NMJs) and found them to positively correlate with the number of Q72-mCherry aggregates in the myotubes. Second, we found that depolarization of neurons by KCl, led to increased transmission of aggregates from neurons to muscles. Interestingly, synaptic density and neuronal depolarization also elevate cell-to-cell transmission of Tau[11]. Therefore, a transsynaptic transmission pathway might cause a continuous increase in toxic protein concentration and thus the presence of a high number of synaptic connections in the nervous and skeletal muscle system might make these structures particular vulnerable to disease[35,43].

We further have assessed NM transmission of mHTTEx1Q72 with three different neuronal clones, each expressing the transgene at different levels. Co-cultures with the lowest expressing line (Neu Q72-Cre) showed no EM48+ aggregates in the neurons at time-points of NM transmission DCC 7 to 21. Only very few Em48+ aggregates could be detected at DCC28 in GFP+ myotubes. This thus strongly suggests that the misfolded mHTTEx1 is transmitted in a non-aggregated form, potentially as smaller mono- or oligomeric structures. Pointing in the same direction was the temporal analysis of aggregate size in muscles co-cultured with HTTEx1Q72-mCherry neurons. Large aggregates with volume above 1μm^3 provided a minor fraction at DCC7 (11%) and increased to 46% at DCC 14. At DCC21 there was an increase in aggregate size above 5μm^3 suggesting gradual aggregation. At the same time the largest increase in absolute numbers at all-time points was for aggregates with volumes below 1μm^3, suggesting that small mHTTEx1 assemblies are the major transmitted form. Furthermore, we found that transmission gradually increases with higher expression levels of Q72-mCherry (comparison between co-cultures with Neu Q72-mCherry Cl#72 (low) and #75 (high)), which suggests that protein concentration drives transmission. Thus the efficiency of transmission is dependent on multiple factors, including cell-to-cell connectivity, neuronal activity, toxic protein concentration and as shown by Kim et. al. polyQ length[17]. A progressive decline of structure and function of the nervous and skeletal muscle system together with an increase in toxic protein aggregation might make this pathway particular relevant to earlier, preclinical stages of disease. In clinically late-onset neurodegenerative diseases, like HD, a potentially low-level, but across many years' continuous transmission of mHTTEx1 might importantly contribute to the formation of intracellular aggregates at later stages of the disease.

Pathological consequences of trans-neuromuscular transmission of N-terminal mHTTEx1

An important question in the field is the contribution of the misfolded protein transmission to disease pathology. Misfolded proteins like tau, α-synuclein and mHTT have a high affinity for lipid membranes. The interaction of these proteins with the membrane accelerates their aggregation and might cause decreased mobility and mislocalization of membrane receptors important for cell signaling and neuro- and neuromuscular transmission[47-52]. Using the Imaris surface model applied to muscle cells, we revealed that at DCC15 and 21 more than 50% of aggregates localized to the surface and for aggregates with volume above 5μm^3 it was nearly 100%. Thus, mHTTEx1 transsynaptic transmission might cause a local increase in mHTTEx1 concentration at the cellular surface which creates an aggregation nucleation side[47]. Interestingly, Harjes and Wanker, 2013 have described the localization of mHTT to several subcellular compartments in neurons, including the dendritic plasma membrane[52]. The dendritic plasma membrane contains the postsynaptic side of a neuronal synapse, as is the myotube surface in a neuromuscular synapse. When we increased the influx of aggregates to the muscles by depolarization of neuronal cells with KCl we observed 2 hours after the treatment proportionally less aggregates in proximity to the surface compared to inside, suggesting that there is an intracellular turnover of aggregates. We may speculate that the entrance of mHTTEx1 into the cells facilitates their interaction with the cell membrane where pathological aggregation with time takes place. It remains to be further investigated what kind of mechanism is regulating intracellular localization of aggregates and what pathological consequences aggregates may have for the membrane permeability and functionality.

Next, we assessed the pathological effect of mHTTEx1 NM transmission on myotubes in both the presence and the absence of autonomous mHTTEx1 expression in myotubes. To do so we compared the cell autonomous versus non-cell autonomous (transmission) effect of mHTTEx1 on mitochondria structure, myotube contraction parameters and formation of nuclear aggregates. Muscular mitochondria morphology was more affected when myotubes were co-cultured with Q72-mCherry neurons comparing to myotubes autonomously expressing the toxic construct and resembled mitochondrial fragmentation. In HD patient brains mitochondrial fragmentation is believed to be caused by an association of stabilized HTT oligomers with mitochondrial proteins resulting in defective axonal transport of mitochondria and synaptic degeneration[53,54]. Furthermore, mitochondrial dysfunction in HD results in reduced ATP levels and likely contributes to muscle fatigue measured in HD patients already at preclinical stages of disease[27,29]. We found that myotube contraction activity and total area was from DCC15 onwards reduced in co-cultures where mHTTEx1 was expressed in neurons (transmission), compared to cell autonomous expressing co-cultures and that the reduction was increased with higher expression levels of the mHTTEx1 protein in neurons. Interestingly, Myo Q72 showed larger contraction parameters than Myo control. This together suggests that synaptic transmission affects different cellular properties than cell autonomous expression of mHTTEx1, resulting in a transmission-selective and cell autonomous-selective functional phenotype. Neu Q72-Cre and Neu Q72-mCherry, cl#75 both developed an repetatetive AP firing pattern, therefore the reduced contraction parameters in co-cultures with transmission compared to those w/o suggests that mHTTEx1 transmission impairs NMJ function. In three studies by Waters et. al., 2013, Miranda et. al., 2017 and Khedraki et. al., 2017 they observed in R6/2 mice a hyperexcitable muscle phenotype and reduced neuromuscular transmission in the absence of obvious nerve denervation[55-57]. They suggest that the

hyperexcitable muscle phenotype might develop to compensate for the reduced NMJ transmission. Our study reveals now that these two phenotypes are likely developing independent from each other. Cell autonomous expression versus transmission of toxic proteins might both result in a local intracellular increase of toxic protein, each targeting different subcellular compartments, this could explain the occurrence of selective functional phenotypes as observed in our study.

Potentially, the impairment in NMJ function found in our study is caused by an identified here association between the larger HTTEx1Q72-mCherry aggregates and the AChRs in NMJs. In contrast, cell autonomously expressed mHTTEx1 may have a more prominent cytoplasmic and/or nuclear localization and possibly affects gene transcription resulting in altered expression of for example chloride and potassium inward rectifying channels, which mRNA levels have been found to be reduced in R6/2 mice[56].

As a third HD-related pathology, we analyzed the extend of nuclear aggregates. N-terminal fragments of HTT have been found in nuclear inclusion bodies in HD patients, and represent a hallmark of HD[23]. We found that nuclear localization of aggregates was increased in co-cultures where both neurons and muscles expressed mHTTEx1, compared to co-cultures with expression selectively in either neurons or myotubes.

Taken together, the above data provide evidence that HTTEx1Q72 trans-NMJ transmission results in pathological alterations in muscle cells, which aggravates in the presence of myotube autonomous HTTEx1Q72 and with increased HTTEx1Q72 protein concentration in neurons. The latter might be relevant to disease, because due to for example, a decline in the protein clearing machineries and cell-to-cell transmission of the toxic proteins, the pathogenic protein concentrations are likely to increase with disease progression.

Last, but not least it is important to mention that even though HTT is generally considered to be ubiquitously expressed in the body, the human protein data bank shows that skeletal muscles of healthy subjects do not express the HTT protein, despite the presence of HTT mRNA[41]. We also did not detect *full-length* HTT protein in skeletal muscle in contrast to its presence in whole brain and cortex tissue samples of *wild-type* mice. Bringing a possibility that the transmitted mHTTEx1 considerably contributes to the muscle pathology in HD. However, it might also be that aberrant translation of the mRNA occurs in HD muscle, resulting in cell autonomous mHTT protein.

Altogether, our *in vitro* and *in vivo* data support the hypothesis that a slow, but continuous neuromuscular transmission of mHTTEx1 in HD patients might result in a steady increase in toxic protein load in muscle cells, which likely will gradual worsen muscle function in HD patients. In a broader context, transsynaptic transmission of misfolded proteins, including mHTT, tau, α-synuclein and tdp-43 is likely the main pathway through which these toxic species spread through the brain and thus, this mechanism might also contribute to a decline of neuronal function over time. Therefore, a better understanding of the molecular mechanism is of high importance for the development of novel therapeutic strategies with the goal to delay and / or slow down dysfunction of both the peripheral skeletal muscles and the central nervous system.

Materials and Methods

iPSC culture and characterization

iPSCs were previously generated from healthy adult human dermal fibroblast lines from a 32-year-old female from Invitrogen (C-013-5C), as described before (31). In brief, iPSCs were maintained on Matrigel (354277, Corning) coated dishes with mTeSR 1 medium (05851, Stemcells Technologies) supplemented with Pen/Strep 1% (15070-063, ThermoFisher). Before differentiation, iPSCs were confirmed to be pluripotent by western blot with OCT4 pluripotency marker (Supplementary Fig. 1c).

Generation and differentiation iND3 Neurons:

Neuronal differentiation protocol is described in Russell et al. (31) with smaller modifications. Briefly, iPS cells were plated on matrigel in proliferation medium composed of DMEM/F12 with Glutamax (10565-018, Gibco) supplemented with 2% B27(17504-044,ThermoFisher) and 1% N2 (17502-048,ThermoFisher), 1% Pen/Strep (15070-063, ThermoFisher) supplemented with 10 ng/ml hEGF (PHG0315, ThermoFisher), 10 ng/ml hFGF (CTP0263, Invitrogen), with 10 µM Rock inhibitor (RI) for 1 day and 1 µg/ml doxycycline for 3 days, then progenitors were kept frozen in Cryostor freezing medium (07930, STEMCELL technology) or replated for immediate experiments.

Generation of *MyoD* iPSCs and differentiation to iMD3 myoblasts:

Human MyoD cDNA was synthesized using sequence information from the Ensembl database (Accession number NM_002478) and cloned under the control of TRE tight (Tetracycline Response Element) promoter in a PiggyBac/Tet-ON all–in-one vector (Lacoste 2009). This vector contains a CAG rtTA16 cassette allowing constitutive expression of Tet-ON system and an Hsv-tkNeo cassette for generation of stable IPS clones. Genereation of MyoD iPS was performed following a previously published protocol (Russell 2018). Briefly, 1×10^6 iPS cells were nucleofected by Amaxa nuclefector device using Human Stem Cell Nucleofector® Kit 1 (VPH-5012, Lonza) and program B-016 with 4 µg of MyoD plasmid and 1 µg of the dual helper plasmid. Subsequently cells were replated on matrigel plates with NutriStem medium containing 10 µM of Rock inhibitor. Antibiotic selection (G418 0.1 mg/ml) was applied after 48 hours. Stable clones appear within 1 week.

MyoD iPS cells are seeded on 5µg/ml laminin-521-coated (Biolamina) in 5% KSR medium composed of Alpha-MEM (12571-063, Gibco), 5% KSR (10828028, Gibco), 1% Pen/Strep (15140-122, Gibco), 100µM β-Mercaptoethanol (21985-023, Gibco) + 1µg/ml DOX + 10 µM RI for 1 day. Medium change with 5% KSR medium + 1µg/ml Dox was done 24h later. 3 days after seeding, cells were frozen in Cryostor freezing medium or replated. Here, they are named iMD3 (iPS-derived myoblasts Day 3). (Supplementary Fig. 2a).

Plasmids generation

The human Huntingtin Exon1 carrying pathological 72 glutamines is fused to the Cre recombinase sequence (HTT_Ex1Q72-Cre) or mCherry (HTT_Ex1Q72-mCherry) under the CAG promoter in a PiggyBac (PB) plasmid. A second PB plasmid is designed to carry a lox-stop-lox_GFP sequence (under the same CAG promoter). HTT_Ex1Q72-Cre, HTT_Ex1Q72-mCherry, lox-stop-lox_GFP contructs were obtained by gene synthesis and cloned into PB backbone by Life

Technology Europe BV.The three PB plasmids were nucleofected in iPS Ngn2 or iPS MyoD as described next.

Generation of Cre-, mCherry and LoxPP- stable lines

A single cell suspension of iPS is collected upon Tryple Express Enzyme (12604-013, Gibco) detachment (5' at 37°C). 1×10^6 cells were resuspended in 100 µl of the nucleofection hESC solution 1 (Human Stem Cell Nucleofector® Kit 1/ Lonza #VPH-5012) where 5 µg of plasmids were added previously: 4 µg PB construct 1 µg Dual helper (expressing transposase). Nucleofection was performed using program B-016 on the Amaxa nucleofector II. Cells were immediately seeded after transfection into 6cm matrigel-coated dishes containing mTESR1 medium supplemented with 10 µM RI. 1µg/ml Puromycin selection is started 48-72h later. Clones were picked after 10 days. The clone was seeded in a new matrigel coated-35mm dish to amplify the new stable lines.

The stable lines were tested by temporal transfection with either the Q72-Cre construct in LoxPP-GFP cell line and vice versa. Fluorescence was monitored daily with EVOS microscope to check their functionality. In parallel, the presence of HTTEx1Q72-Cre or HTTEx1Q72-mCherry was checked via Western blot using Mab5492 antibody.

From iMD3 to neuromuscular on-top coculture for live imaging

iMD3 cells were thawed (or replated) on laminin521- coated plates with 5% KSR medium+20ng/ml hFGF (CTP0263, Invitrogen) + 10µM RI for 3days with a seeding density of 2.5×10^6 cells per laminin-521-coated 10cm dish. Medium change was done 24h later without RI. After 3 days from seeding, the 10cm dish was confluent. Cells were detached with Tryple Express Enzime (12604-013, Gibco), counted and seeded in medium C composed of DMEM F12-Glutamax + 5% FBS (SH30070.02, HyClone)+ 0.35% BSA (A1595, Sigma)+ 1%Pen/strep+ ITS 1:500 (354351, BD)+ 2µM CHIR99021 (1046, Sigma)+ 1µM Dorsomorphin (04_0024, Stemgent) + 1mM Dibutyryl-cAMP (BS0062, Biotrend) + 1µg/ml DOX + 10µM RI , and 2×10^5 cells per well were seeded on laminin-521-coated 96 well IBIDI µ-plate (89626, IBIDI). RI and DOX was removed after 1 day. Medium was changed every other day until day 7 after seeding.

iND3 are thawed and seeded on top of the myotubes culture. 1.8×10^5 iND3 are plated in neuronal differentiation medium composed of Neurobasal Medium (21103049, Thermofisher) + B27 with Vit. A (17504-044, Invitrogen) + N2 supplements (17502-048, Invitrogen) + Pen/Strep/Glutamax 1% supplemented with BDNF, GDNF, hNT3 (all from R&D at 10 ng/ml). Starting from day 2 of co-culture, medium change was done every other day.

Neuromuscular cocultures were imaged at day 4, 7, 14, 21, 28 with Operetta (Perkin Elmer) in live-cell imaging (37 °C, 5% CO_2) with 10x (NA 0.4) objective. GFP positive cells were counted manually.

Electrophysiology

Neuromuscular co-cultures were established on glass in 24-well plates with a density of 3×10^5 hiPSC-derived iNgn2 (control, Neu Q72-Cre or Neu Q72-mCherry cl.#75) neurons and 1.5×105 hiPSC-derived iMyoD LoxP-GFP myotubes. The whole-cell patch-clamp technique was used to record action potentials of neurons at day of co-culture 7, 14 and 21. Co-cultures were taken from the incubator and transferred to the recording chamber with artificial cerebral spinal fluid (ACSF)

containing (in mM): 125 NaCl, 25 $NaHCO_3$, 2.5 KCl, 1.25 NaH_2PO_4, 2 $MgCl_2$, 2.5 $CaCl_2$ and 11 glucose, pH 7.4, constantly bubbled with 95% O_2 and 5% CO_2; 315–320 mOsm. The cells were kept at 30 - 32 °C and allowed to adapt for 20 minutes prior to recordings. Neurons were visualized with a LNScope (Luigs & Neumann) equipped with an oblique illumination condenser, a 60x objective (LUMPplanFI, NA 0.9) and a reflected illuminator (Olympus). Patch electrodes (5–7 MΩ) were pulled from borosilicate glass tubing and filled with an intracellular solution containing (in mM): 125 K-gluconate, 20 KCl, 10 HEPES, 10 EGTA, 2 MgCl2, 2 Na2ATP, 1 Na2-phosphocreatine, 0.3 Na3GTP, pH 7.2 (with KOH); 312.3 mOsm. Current-induced action potentials were recorded (with a holding potential of −70 mV) using a Multiclamp 700B amplifier (Molecular Devices) and digitized at 10 kHz. Recordings were performed at 30 – 32 °C in oxygenated ACSF. Igor Pro software (version 6.3, Wavemetrics) was used for both data acquisition and off-line analysis.

Cell culture inserts

Culture-Insert 2 Well from IBIDI (81176) were used to seed iND3 and iMD3 in spatially separated areas of the well. Cell densities were adapted to this format. iND3 were seeded on Poly-L-lysine (P1524, Sigma) and laminin-521, iMD3 were seeded on laminin-521. Cells were monitored with EVOS M7000 microscope at day 1, 4, 8, 15 after the removal of the culture insert to check for the presence of GFP cells.

Contractility assay in on-top co-culture

The primary readout for the amount of contraction in any on-top co-culture was captured as the total amount of motion within any given field of view over time. The Yokogawa CV7000 microscope with a 10x objective (NA 0.3) was adopted for this assay. The raw images were acquired as a series of 2560x2180 16-bit grayscale brightfield images with a frequency of 2 Hz., for a total amount of 60 images per field with 4 fields of view in each well. This assay was performed in live cell-imaging conditions (37°C, 5%CO_2). At least 3 wells per experimental condition were acquired and analyzed.

For each consecutive pair of image frames a motion field was computed which provides, for each pixel location, a direction and magnitude of projected spatial motion. Thus, for N image frames we obtained N-1 motion frames. A numerical threshold on the magnitude of the motion vectors was applied to eliminate possible noise and vibration artefacts and to obtain a reliable binary image map of region-of-contraction. The union of all such pixels over all motion frames in the time series was computed and used as the final region-of-contraction map for comparative analysis between cell lines or treatments. These values were used to describe the on-top co-culture functionality as follows:

- Total contracting area normalized to well area (%): sum of moving pixels normalized to the acquired fields area (namely, sum of the pixels occupied by the 4 fields of view)
- Active images per well normalized to total number of images (%) where active image are images for which a pixel movement was detected

Antibodies and dyes:

For western blot: 1:500 Embryonic myosin (MHC3) (F1.652, DHSB), 1:500 Postnatal myosin (MHC8) (N3.36, DSHB), 1:1000 Islet 1(AF1837-SP, R&D), 1:2000 Doublecortin (DC) (4604, Cell

signaling), 1:1000 Choline acetyltransferase (ChAT) (AB144P, Merck) 1:250 Oct4 (09-0023, Stemgent), 1:5000 GAPDH (ab9485, abcam), 1:5000 β-actin (A5441, Sigma), 1:5000 MAB5492 (MAB5492, Sigma-Aldrich),
For immunofluorescence: Hoechst 33342, 5µg/ml α-bungarotoxin (B1196, Thermofisher), 1:2000 Bassoon (141 013, Synaptic Systems), 1:1000 Neurofilament M (171 204, Synaptic systems); 1:1000 Myosin Heavy Chain 1 (05-716, Millipore), 1:5000 mCherry (ab205402, Abcam) 1:500 TOMM20 (ab186735, Abcam), 1:500 EM48 (MAB5374, Merck) , 1:100 ChAT (AB144P, Merck), 1:2000 Map2 (ab5392, Abcam), 1:800 V5 (D3H8Q, Cell Signaling), 1:40 NF2H3 (AB2314897, DSHB).All the secondary antibodies were Alexa conjugated and used 1:1000 for 1 h at RT.

Immunocytochemistry for GFP+ cells

Cells were fixed in 4% paraformaldehyde (PFA) at room temperature for 7 min, followed 3 DPBS (14190, Sigma-Aldrich) washings, five minutes each. DPBS supplemented with 0.1% Triton X-100 (for permeabilization) and 1% BSA (blocking) was used for primary antibodies labelling, overnight at 4°C . After three washing steps with DPBS, cells were incubated for 1h with secondary antibodies (Invitrogen). Afterwards, cells were washed in DPBS and incubated with Hoechst 33342 in ddH2O for 10min. Ibidi mounting medium (50001, IBIDI) is added to the wells and stored at 4°C. Images were acquired with LSM900 microscope with Plan-Apochromat 63x/1.40 Oil DIC M27, using Zen 3.2 (Blue edition) software.

Western Blot

IPSC-derived neurons, myotubes or co-culture cells were harvested at different time points, washed twice with ice-cold PBS, and subsequently lysed in RIPA buffer supplemented with complete EDTA-free protease inhibitor mixture (11873580001, Roche). Lysates were incubated on ice for 15 min and cleared via centrifugation (10,000 × g) for 10 min at 4 °C. Supernatants were collected, and the protein concentration was determined using a BCA assay kit (Thermo Scientific Pierce, 23227). Lysates were resolved using standard SDS-PAGE gels and after blocking, blots were incubated with primary antibodies overnight at 4 °C. After washing, blots were incubated with secondary antibodies and visualized using SuperSignal Femto chemiluminescent detection kit (Thermo Scientific) in Odyssey Infrared Imager (LiCor, 9120). ImageJ was used for densitometry measurements.

Immunofluorescence on coverglass culture

Cells on glass coverslips (in format 24 well plate with 300,000 myotubes and 300k neurons density) were fixed for 5 min in 4% PFA/4% sucrose at RT, permeabilized with PBS+/+ (D8662, Sigma, supplemented with 1 mM MgCl2 and 0.1 mM CaCl2)/Triton-0.1%, blocked with 5% BSA in PBS+/+ and labeled with primary antibodies in PBS+/+ (D8662, Sigma) and 5% BSA overnight at 4°C and secondary antibodies for 1h RT. PBS+/+ washes were performed after each antibody incubation. Coverslips were mounted on glass slides in Prolong (P36930, Invitrogen).

Microfluidic devices (MFD) culture.

We used XonaChips XC450 devices from Xona Microfluidics. iMD3 cells were growth in 5%KSR medium (Alpha-MEM (12571-063, Gibco); 5% KSR (10828028, Gibco); 1% Pen/Strep (15140-122, Gibco); 100µM β-Mercaptoethanol (21985-023, Gibco), supplemented with 1µg/ml

doxycycline (D1822, Sigma) and 20ng/ml FGF (300-112P, Gemini Bio). At DIV 3 the cells were seed in final format for differentiation: In myocytes side, 300,000 cells were seed and in the neuronal side, 1.5 × 10^5 cells in 5 µl medium, were seeded to give support to the motor neurons. The myotubes growth for 7 days in "Differentiation medium" (DMEM F12-Glutamax (10565-018, Gibco); 5% FBS (SH30070.02, HyClone); 1:500 ITS (354351, BD); 0.1% BSA (A1595, Sigma); 1% Pen/Strep, supplemented with 2µM CHIR99021 (1046, Sigma); 1 µM Dorsomorphin (04_0024, Stemgent); 1mM Dibutyryl-cAMP (BS0062, Biotrend). Then, 300,000 neurons were seeded in the neuronal compartment and the culture growth in "neuronal medium" (Neurobasal TM Medium; B27 (17504-044, Invitrogen); N2 supplement (17502-048, Invitrogen) 1% Pen/Strep/Glutamax; and BDNF, GDNF, hNT3 (all from R&D).
For immunofluorescence experiments, the culture was fixed at different time points for 10 min in 4% PFA/4% sucrose at RT, then the immunofluorescence protocol was followed.

Mitochondrial Morphology Quantification
Mitochondrial shape parameters were quantified using the open-source software package ImageJ and as previously described (Merrill R.A., Flippo K.H., Strack S. (2017) Measuring Mitochondrial Shape with ImageJ. In: Strack S., Usachev Y. (eds) Techniques to Investigate Mitochondrial Function in Neurons. Neuromethods, vol 123. Humana Press, New York, NY. https://doi.org/10.1007/978-1-4939-6890-9_2) Briefly, images were background-subtracted (rolling ball radius = 50 pixels) and uneven labeling of mitochondria was improved through local contrast enhancement using contrast-limited adaptive histogram equalization ("CLAHE"). To segment mitochondria, the "Tubeness" filter was applied. After setting an automated threshold, the "Analyze Particles" plugin was used to determine the area and perimeter of individual mitochondria and the "Skeletonize" function was used to measure mitochondrial length.
Three parameters were assessed:
- Mitochondrial length: the length reports the mitochondrial length or elongation in pixel, after the mitochondria are reduced to a single-pixel-wide shape ("Skeletonize" function on ImageJ).
- Form factor (FF): The FF value describes the particle's shape complexity of the mitochondria, as the inverse of the circularity.
- Area-weighted form factor (AWFF): a variant of FF with a bias towards larger mitochondria or mitochondrial networks. AWFF provides more realistic results in cases where highly elongated mitochondria are overlapping

Animal husbandry
Adult NEX-Cre were kindly provided by Dr. Sandra Goebbels (Max-Planck-Institute of Experimental Medicine, Goettingen, Germany). All mice were housed in temperature (22°C) and light-controlled environment on a 12-light dark cycle and had access to food and water ad libitum. All experimental procedures were carried out according to Basel University animal care and use guidelines. They were approved by the Veterinary Office of the Canton of Basel-Stadt, Switzerland.

Delivery of viral vectors
Four-week old female NexCre mice were anaesthetized by the administration of 4% isoflurane, were maintained under isoflurane anesthesia (1-2%) and kept warm with a heating pad (53800,

Stoeling). The head was fixed to a stereotaxic frame (Kopf Instruments) with ear bars and the skin was disinfected with 70% ethanol and polyvidone iodine. The skin was cut with surgical scissors to expose the skull, allowing the identifications of bregma and lambda. Using a borosilicate glass pipette and a pressure ejection system (Eppendorf) 250 nL of the self-complementary AAV-9/2-DIO-mHTTExon1Q138-V5 (VVF, Zürich) were injected in the layer V of the primary motor cortex, using the following coordinates AP (anterior-posterior): + 1.18, ML (medial-lateral): + 2.00, DV (dorsal-ventral): + 2.00, according to the Paxinos and Franklin mouse brain atlas (Paxinos and Franklin, 2019). The mice were placed in a recovery cage to awaken before returning to their home cage. 6 month old female mice were anesthetized by the administration of 4% isoflurane and were fast decapitated.

Immunohistochemistry for spinal cord and muscle samples.

The spinal cord, biceps and triceps were dissected on ice and embedded in low-melting agarose (16520050, ThermoFisher Scientific). Samples were sliced in 100µm thick sections using a vibratome (VT1200, Leica). Then, fixed in 4% paraformaldehyde (PFA) at room temperature for 10 min, followed by 3 DPBS (14190, Sigma-Aldrich) washings, 10 minutes each. DPBS supplemented with 0.1% Triton X-100 (for permeabilization) and 1% BSA (blocking) was used for primary antibodies labelling, for at least 2 days at 4°C. After three washing steps with DPBS, cells were incubated for 3h with secondary antibodies (diluted 1:800, Invitrogen). Afterwards, cells were washed in DPBS for 3 times. Sections were then mounted on glass slides using ProLong Gold (P10144, ThermoFisher Scientific) and acquired with LSM800 with 40x objective (ZEISS, EC Plan-NEOFLUAR 40X/1,3 Oil)

Image acquisition and analysis

Fluorescence signals in “on top” culture for iPSC-derived co-culture were imaged with Zeiss LSM-700 system with a Plan-Apochromat 40 × /NA 1.30 oil DIC, using Zen 2010 software. For bin analysis in MFD, section of 0-160, 160-320 and 320-480 µm were taken in the using Zeiss LSM-800II inverted system with a Plan-Apochromat 40 × /NA 1.30 oil DIC, using Zen blue 2.6 software. Whole-cell, 16-bit stacks images with 0.33-µm step size were acquired (15–30 planes). Immersion oil with 1.518 refractive index at room temperature was applied to the lens. Coverslips were mounted with ProLong Gold anti-fade reagent (P36930, Thermofisher) with a refractive index of 1.46. All images were acquired with identical microscope settings within individual experiments. Brightness and contrast were adjusted equally for all images, and cropped insets were generated in the same manner among all the experiments to facilitate visualization of representative cells. Saturation was avoided by using image acquisition software to monitor intensity values. For any image adjustment, identical settings were always applied to all cells, irrespective of genotype. Cells that were clumped or overlapping were excluded from quantification. For quantification, values were averaged over multiple cells from at least three independent culture preparation.

Quantification of HTTEx1Q72 mCherry was done using Image J software. Images were background subtracted and after setting an automated threshold, the “Analyze Particles” plugin was used to determine the number and area of aggregates localized in MHC+ staining. Arbitrary, were consider aggregates “particles” between 0.2-5 μm^2.

Quantification of nuclei (Dapi staining) containing HTTEx1Q72 mCherry were done using Image J software. Images were background subtracted and after setting an automated threshold,

the “Analyze Particles” plugin was used to determine the number of nuclei. Round nuclei in MHC1 negative staining were consider from neurons and were not consider for quantification.
Integrated density of EM48/MAP2+NF staining was done using Image J software. Images were background subtracted and after setting an automated threshold, integrated density was measured in the full image, to consider EM48 staining in the soma and neurites of the neurons. The values were normalized to the neuronal market MAP2 and NF.

AChR clusters were analyzed using Imaris Software (v.9.6.0; Oxford Instruments) based on immunofluorescent images acquired by Confocal microscope. 3D reconstruction of AChR and Bassoon structures were done using Imaris surface function. Automatically generated values for volume and sphericity were used to characterize the clusters. Only structures with volume above 0.02 and below 20 μm^3 were analyzed for Bassoon and only structures above 0.024 μm^3 for AChR. Distances between the surfaces provided by Imaris software were used to identify AChR cluster and Bassoon association. Association was defined as distance below 0.05 µm.

Aggregates volume was analyzed by Imaris surface function and volume measurement based on mCherry fluorescence staining. Aggregates with volume above 0.02 and below 30 μm^3 and localized within the surface generated based on MHC1 staining were analyzed.
Intracellular localization of aggregates was analyzed using distances between surfaces generated based on mCherry staining for aggregates and MHC1 staining for muscle by Imaris software. Localization at the surface was defined as distance between 0 and 0.05 µm.

Multiple images were analyzed using Imaris Batch function. The data on volume, sphericity and distances between the surfaces were exported and further analyzed using R (v.4.0.5;https://www.R-project.org/) and RStudio software (v.1.4.1106, https://www.rstudio.com/).

Statistical analysis

Data analysis was performed with GraphPad Prism version 8.0 (GraphPad Software, La Jolla, CA) and using R software (v.4.0.5; https://www.R-project.org/). Individual data sets were tested for normality with the Shapiro-Wilk, D’Agostino & Pearson or Kolmogorov-Smirnov test. Statistical significance of differences between groups was assessed by unpaired two-tailed Student’s t-test or ANOVA as indicated. For data with non-normal distribution the non-parametric Mann–Whitney or Kruskal-Wallis tests were used. For comparison on group proportions Chi square test or Fisher’s exact test (for samples with expected frequencies below 5) were used. p-values < 0.05 were considered significant. Data are presented as mean ± standard error of the mean (s.e.m.).

Acknowledgements

We thank Dr. Enrique Pèrez-Garci for establishing and expert training on the electrophysiology and stereotactic injection technology in the laboratory. We thank Patricia Valerio (from Prof. Dr. Tania Barkat lab) from the Department of Biomedicine (DBM), University of Basel, for providing us further training with the stereotactic injection technology. We also thank the Dr. Michael Abanto from the imaging facility of the DBM, University of Basel and Alexia Loynton-Ferrand from the imaging facility of the Biocenter, University of Basel for their expert training on imaging acquisition and analysis. Furthermore, we thank Inga Galuba and Isabelle Claerr from Novartis Institute of

Biomedical research (NIBR), Basel, for their technical support with the Yokagawa imaging technology and Dr. Gianluca Santarossa from NIBR, Basel, for his expert help with the analysis of the myotube contraction data obtained from the Yokagawa image acquisition. We are also grateful to Prof. Josef Bischofberger, DBM, university of Basel, for his support and discussions on the project. This work was supported by a Swiss National Science Foundation professorship grant (PP00P3_163937; PP00P3_194806) and a Synapsis foundation – Alzheimer Research Switzerland ARS grant for principal investigators to EPV.

Figure legends

Figure 1: Transmission of HTTEx1Q72 from neurons to muscle cells in hiPSC-derived neuromuscular co-cultures. **a**) Schematic of the experimental approach to follow in parallel, for multiple weeks, the development of functional neuromuscular junction activity and transmission of HTTEx1Q72-cre expressing neurons to Myotubes bearing a LoxP-GFP sequence by live-cell, high-throughput imaging. **b**) Western blot showing the expression of developmental markers for myotubes (MHC3 = embryonic myosin, MHC8 = postnatal myosin) and for motor neurons (DC, Islet1 and ChaT) at increasing DCC. **c**) IF images visualizing the morphological presence of neuromuscular synapses (depicted in top right image: orthogonal view of presynaptic active zone marker Bassoon in close apposition to the postsynaptic marker BgTx (labels the AChRs on myotubes) in Neu Q72-Cre / Myo LoxP-GFP co-cultures at DCC21. NFM labels the axons and MHC1 is a pan-myosin marker. **d**) Graph displays percentage of Neu Q72-Cre with either a phasic, adaptive or tonic type of current-induced AP firing pattern or no AP firing (none) under voltage-clamp of the neurons at -70mV, at DCC 7, 15 and 21. **e**) Quantification of the percentage of images with myotube contractions (left graph) and total myotube contracting area obtained from 1-well of a 96-well plate, at increasing DCC (n=3) (% of total myotube contracting area was measured at each time point and the values are here listed as mean ± s.e.m. Neu Q72-Cre / Myo Ctr, DCC2: 0.033 ± 0.01; DCC8: 0.054 ± 0.016; DCC15: 0.149 ± 0.018; DCC22: 0.553 ± 0.145; DCC29: 0.761 ± 0.153 and Myo Ctr, DCC2: 0.007 ± 0.0003; DCC8: 0.004 ± 0.001; DCC15: 0.007 ± 0.004; DCC22: 0.016 ± 0.011; DCC29: 0.015 ± 0.011. % of active images was calculated at each time point and the values are here listed as mean ± s.e.m. Neu Q72-Cre / Myo Ctr, DCC2: 8.333 ± 2.386; DCC8: 10.00 ± 1.713; DCC15: 20.00 ± 2.261; DCC22: 30.56 ± 5.283; DCC29: 35.00 ± 2.132 and Myo Ctr, DCC2: 2.5 ± 0; DCC8: 1.389 ± 0.6054; DCC15: 1.111 ± 0.439; DCC22: 1.111 ± 0.605; DCC29: 0.833 ± 0.416. **f**) A live-cell fluorescent image obtained with the Operetta high-throughput imaging system revealing GFP+ myotubes at DCC 4 and 28 (Arrowhead indicating a GFP^+ myotubes at DCC4). **g**) Quantification of the number of GFP+ myotubes in a Neu Q72-Cre / Myo LoxP-GFP co-culture at increasing DCC. **h**) Orthogonal view of an IF image showing an Em48+ HTT aggregate in the cytoplasm of a GFP+ myotube. Hoechst (blue) labels the nuclei. Abbr: **AChRs** = acetylcholine receptors; **BgTx** = α-bungarotoxin (used to label the AChRs throughout the paper) ; **ChaT** = choline acetyltransferase; **DC** = doublecortin; **DCC** = days of co-culture; **IF** = immunofluorescence; **MHC** = myosin heavy chain; **NFM** = neurofilament M.

Figure 2: Transmission of HTTEx1Q72 across the neuromuscular junction in Neu Q72-mCherry cl#75 / Myo co-cultures in MFDs. **a, upper panel**) Schematic of MFD depicting the co-culture setting. Neu Q72-mCherry (white with red dots) are plated in presynaptic chamber and Myo (green) are plated in postsynaptic chamber. Neurons extend their axons through the microgrooves to the myotubes. **a, lower panel**) IF image of mCherry (shown in white) in MFD visualizing Neu Q72-mCherry in presynaptic chamber and extension of their axons to the postsynaptic compartment. **b**) IF images visualizing the morphological presence of neuromuscular synapses (depicted in top right image: orthogonal view of close apposition between Bassoon and BgTx) in Neu Q72-mCherry / Myo co-cultures in MFD at DCC21. **c, left, upper panels**) IF Images depicting the four different types of AChR clusters identified on Myo co-cultured with Neu Q72-mCherry. **c, left lower panels**) Shows Myo surface (green) and Bassoon surface (white) created in Imaris from the IF images shown in top panels. **c, right panel**) Distribution of AChR cluster types in percentage, found on Myo when associated with (+) or w/o (-) Bassoon. χ^2 test. **d**) Percentage of Neu Q72-cre with either a phasic, adaptive or tonic type of current-induced AP firing pattern under voltage-clamp of the neurons at -70mV, at DCC 7, 15 and 21. **e**) IF images of Myo compartment at DCC 7 showing presence of Q72-mCherry+ axons and at DCC21 showing presence of Q72-mCherry+ axons and Q72-mCherry puncta in MHC1+ Myo. **f)** Quantification of the number of Q72-mCherry aggregates in Myo at DCC 7 – 28. One data point corresponds to one image (at least 45 images analyzed per time point, from 1 experimental set). **g**) Volume of individual Q72-mCherry aggregates localized in Myo at DCC 7 – 28. Displayed are the numbers of aggregates in groups corresponding to volume ranges, indicated in the legend. Quantified are aggregates found in Myo across all images from given time point. *** = $p \leq 0.004$ (Kruskal-Wallis).

Figure 3: Trans-neuromuscular transmission of HTTExQ72 is enhanced by increasing NMJ density. **a**) IF image showing NFM+ axons and Q72-mCherry in bin 1, bin 2 and bin 3 of Myo compartment in co-cultures with Neu Q72-mCherry cl#75 at DCC21. **b**) Quantification of the NFM area normalized to the total MHC1 area in each bin. **c**) Quantification of the number of Q72-mCherry aggregates in Myo in each bin. One data point corresponds to one image (12-15 images analyzed per one bin, from 1 experimental set). **d**) IF image showing Q72-mCherry aggregates in MHC1+ Myo with AChR clusters in absence of close appositions to Bassoon (upper panel) or in presence of close appositions between AChR and Bassoon (lower panel) in co-cultures with Neu Q72-mCherry cl#72. **e**) Correlation between number of NMJs (identified as AChR with Bassoon appositions on MHC1+ Myo) and number of Q72-mCherry aggregates in Myo in co-cultures with Neu Q72-mCherry cl#72. **f, left panels**) IF Images depicting the AChR clusters in close proximity (+) (within 0.05 μm) or absence (-) (> 0.05 μm distance) of Q72-mCherry aggregates. **f, right panels**) Distribution of AChR cluster types in percentage when associated (within 0.05 μm) with (+) or w/o (-) Q72-mCherry at DCC 7 – 28. χ^2 test and Fisher's exact test (for DDC 7 and 15 with expected frequencies below 5).

Figure 4: Neuronal depolarization enhances transmission of HTTEx1Q72 from neurons to myotubes in co-cultures with Neu Q72-mCherry cl#72 at DCC 21. **a**) Schematic outline of

experimental approach in MFDs. ACSF with 2.5 mM KCl was added to both the neuronal and myotube compartment for 30 minutes (left schematic). ACSF with 10 mM KCl was added to only the neuronal compartment for 10 minutes (middle schematic). ACSF with 10 mM KCl was changed back to ACSF with 2.5 mM KCl (right schematic). Cultures were fixed after 2 hours. **b**) IF images depicting Q72-mCherry aggregates in MHC+ Myo in cultures exposed to 2.5 mM KCl (control, left panel) and 10 mM KCl (right panel). The inserts correspond to zoom of a representative region. **c**) Quantification of the number of Q72-mCherry aggregates in MHC1+ Myo in control co-cultures and KCl 10 mM treated co-cultures. One data point corresponds to one image (15 images analyzed per condition, from 1 experimental set). **d**) Quantification of the volume of Q72-mCherry aggregates in control and KCl 10 mM treated co-cultures. **e**) Quantification of the distance of the Q72-mCherry aggregates from the MHC1+ surface (created with Imaris surface function) in control and KCl 10 mM treated co-cultures. The number (n) above the (d) and (e) graphs indicates the number of aggregates found in MHC1+ Myo across analyzed images. **** = $p < 0.0001$. Significant difference based on one-way ANOVA.

Figure 5: Overrepresentation of large Q72-mCherry aggregates at the MHC1+ myotube surface. **a**) Overview image of a transparent MHC1+ Myo surface (grey) with Q72-mCherry aggregate surface of those associated with (yellow) and those not associated with (magenta) the MHC1+ surface in co-cultures with Neu Q72-mCherry cl#75. **b, left panel**) Zoom-in image of (a) showing a yellow aggregate penetrating the MHC1+ surface and a magenta aggregate not in contact with the surface. **b, right panel**) Same image as in "b, left panel", but now with closed (non-transparent) MHC1+ surface visualizing only the yellow aggregates on the outside of the MHC1+ surface. **c**) Graphs plotting the distance of Q72-mCherry aggregates to MHC1+ surface against their volume at DCC 7 – DCC 28. **d**) Quantification of percentage of number of Q72-mCherry aggregates at the MHC1+ surface and inside the MHC1+ surface at DCC 7 – 28. The numbers (n) indicate the total number of aggregates analyzed. **e**) Quantification as in (d) for aggregates with a volume larger than 5 μm^3.

Figure 6: *HTTEx1Q72 trans-neuromuscular transmission causes structural and functional pathological alterations in myotubes in a dose-dependent manner.* **a)** Images showing mitochondria marker TOMM20 mask outlining the mitochondria in myotubes in: control (Neu Ctr / Myo Ctr), Myo cell-autonomous (Neu Ctr / Myo Q72-mCh) and transmission (Neu Q72-mCh / Myo Ctr) co-cultures. Associated graphs show the quantification of structural parameters of the mitochondria in these mixed-genotype co-cultures. **b)** Quantification of myotube contraction parameters measured in: control, transmission (with Q72-mCherry cl#75 and Neu Q72-Cre), cell autonomous and transmission + cell autonomous co-cultures at DCC 2 – 29 (Significant difference in the **% of active images** was observed between the following genotype co-cultures: *DCC8*: "Neu Ctr/ Myo Ctr and Neu Q72-mCh / Myo Ctr" ($p = 0.0017$), "Neu Ctr/ Myo Ctr and Neu Q72-mCh / Myo Q72-mCh" ($p = 0.0008$). $p < 0.0001$ for: "Neu Q72-mCh / Myo Ctr and Neu Ctr / Myo Q72-mCh", "Neu Ctr / Myo Q72-mCh and Neu Q72-mCh / Myo Q72-mCh", "Neu Q72-mCh / Myo

Ctr and Neu Q72-Cre / Myo Ctr", "Neu Q72-mCh / Myo Q72-mCh and Neu Q72-Cre / Myo Q72-mCh". *DCC15 and 22*: $p < 0.0001$ for all cultures except between "Neu Ctr/ Myo Ctr and Neu Q72-Cre / Myo Ctr" no significant difference. *DCC 29*: Between all different co-cultures < 0.0001, except between "Neu Ctr/ Myo Ctr and Neu Ctr / Myo Q72-mCh" $p = 0.0014$ and no significant difference between: "Neu Ctr/ Myo Ctr and Neu Q72-Cre / Myo Ctr", "Neu Ctr/ Myo Ctr and Neu Q72-Cre/ Myo Q72-mCh". Significant difference in the **% of total myotube contracting area** was observed between the following genotype co-cultures: *DCC15*: "Neu Ctr/ Myo Ctr and Neu Q72-Cre/ Myo Q72-mCh" $p = 0.045$, "Neu Q72-mCh / Myo Ctr and Neu Ctr / Myo Q72-mCh" $p = 0.0036$, "Neu Ctr / Myo Q72-mCh and Neu Q72-mCh / Myo Q72-mCh" $p = 0.0010$, "Neu Q72-mCh / Myo Q72-mCh and Neu Q72-Cre / Myo Q72-mCh" $p = 0.0001$. DCC22: Between all different co-cultures < 0.0001, except between "Neu Ctr/ Myo Ctr and Neu Q72-Cre/ Myo Ctr", "Neu Ctr/ Myo Ctr and Neu Q72-Cre/ Myo Q72-mCh" no significant difference. *DCC 29*: Between all different co-cultures < 0.0001, except between "Neu Ctr/ Myo Ctr and Neu Q72-Cre/ Myo Ctr" $p = 0.0039$, and no significant difference between: "Neu Ctr/ Myo Ctr and Neu Q72-mCh / Myo Ctr", "Neu Ctr/ Myo Ctr and Neu Q72-Cre/ Myo Q72-mCh". **c)** IF images of: cell autonomous, transmission and transmission + cell autonomous co-cultures at DCC 21 showing Q72-mCherry labeling in dapi (blue) labelled myotubes. The graph represents the quantification of the percentage of myotube nuclei with Q72-mCherry aggregates in in the different genotype co-cultures. * = $p \leq 0.05$; ** = $p \leq 0.01$; *** = $p \leq 0.004$; **** = $p \leq 0.0001$. Significant difference based on one-way ANOVA.

Figure 7: HTTEx1Q72 is transmitted from the motor cortex M1 to spinal motor neurons and skeletal muscles. **a, upper panel**) Image showing stereotactic injection of AAV_LoxP-Q138-v5 in mice expressing Cre specifically in projection neurons, including cortical pyramidal neurons. **a, lower panel**) IF image of Q138-v5 staining at the injection side in the M1 motor cortex. **b**) Q138-v5 aggregates in ChaT+ motor neurons in the brachial spinal cord. **c**) Q138-v5 aggregates in the biceps and triceps forelimb skeletal muscles stained with MHC1. **d**) Western blot showing the expression of full length huntingtin protein recognized with MAB2166 antibody in 100 µg of muscle samples (hindlimbs and forelimbs) and brain and cortex from p7 mice. GAPDH was used as loading control.

References

1 Schmahmann, J. D., Smith, E. E., Eichler, F. S. & Filley, C. M. Cerebral white matter: neuroanatomy, clinical neurology, and neurobehavioral correlates. *Ann N Y Acad Sci* **1142**, 266-309, doi:10.1196/annals.1444.017 (2008).

2 Prusiner, S. B. Novel proteinaceous infectious particles cause scrapie. *Science* **216**, 136-144, doi:10.1126/science.6801762 (1982).

3 Guo, J. L. & Lee, V. M. Cell-to-cell transmission of pathogenic proteins in neurodegenerative diseases. *Nat Med* **20**, 130-138, doi:10.1038/nm.3457 (2014).

4 Vaquer-Alicea, J. & Diamond, M. I. Propagation of Protein Aggregation in Neurodegenerative Diseases. *Annu Rev Biochem* **88**, 785-810, doi:10.1146/annurev-biochem-061516-045049 (2019).

5 Jeon, I. *et al.* Human-to-mouse prion-like propagation of mutant huntingtin protein. *Acta Neuropathol* **132**, 577-592, doi:10.1007/s00401-016-1582-9 (2016).
6 Liu, L. *et al.* Trans-synaptic spread of tau pathology in vivo. *PLoS One* **7**, e31302, doi:10.1371/journal.pone.0031302 (2012).
7 Luk, K. C. *et al.* Pathological alpha-synuclein transmission initiates Parkinson-like neurodegeneration in nontransgenic mice. *Science* **338**, 949-953, doi:10.1126/science.1227157 (2012).
8 Luk, K. C. *et al.* Intracerebral inoculation of pathological alpha-synuclein initiates a rapidly progressive neurodegenerative alpha-synucleinopathy in mice. *J Exp Med* **209**, 975-986, doi:10.1084/jem.20112457 (2012).
9 Masnata, M. *et al.* Demonstration of prion-like properties of mutant huntingtin fibrils in both in vitro and in vivo paradigms. *Acta Neuropathol* **137**, 981-1001, doi:10.1007/s00401-019-01973-6 (2019).
10 Babcock, D. T. & Ganetzky, B. Transcellular spreading of huntingtin aggregates in the Drosophila brain. *Proc Natl Acad Sci U S A* **112**, E5427-5433, doi:10.1073/pnas.1516217112 (2015).
11 Calafate, S. *et al.* Synaptic Contacts Enhance Cell-to-Cell Tau Pathology Propagation. *Cell Rep* **11**, 1176-1183, doi:10.1016/j.celrep.2015.04.043 (2015).
12 Pecho-Vrieseling, E. *et al.* Transneuronal propagation of mutant huntingtin contributes to non-cell autonomous pathology in neurons. *Nat Neurosci* **17**, 1064-1072, doi:10.1038/nn.3761 (2014).
13 Wang, Y. *et al.* The release and trans-synaptic transmission of Tau via exosomes. *Mol Neurodegener* **12**, 5, doi:10.1186/s13024-016-0143-y (2017).
14 Braak, H. & Del Tredici, K. Alzheimer's pathogenesis: is there neuron-to-neuron propagation? *Acta Neuropathol* **121**, 589-595, doi:10.1007/s00401-011-0825-z (2011).
15 de Calignon, A. *et al.* Propagation of tau pathology in a model of early Alzheimer's disease. *Neuron* **73**, 685-697, doi:10.1016/j.neuron.2011.11.033 (2012).
16 Rey, N. L., Petit, G. H., Bousset, L., Melki, R. & Brundin, P. Transfer of human alpha-synuclein from the olfactory bulb to interconnected brain regions in mice. *Acta Neuropathol* **126**, 555-573, doi:10.1007/s00401-013-1160-3 (2013).
17 Kim, D. K. *et al.* Cell-to-cell Transmission of Polyglutamine Aggregates in C. elegans. *Exp Neurobiol* **26**, 321-328, doi:10.5607/en.2017.26.6.321 (2017).
18 Turner, C., Cooper, J. M. & Schapira, A. H. Clinical correlates of mitochondrial function in Huntington's disease muscle. *Mov Disord* **22**, 1715-1721, doi:10.1002/mds.21540 (2007).
19 Zielonka, D., Piotrowska, I., Marcinkowski, J. T. & Mielcarek, M. Skeletal muscle pathology in Huntington's disease. *Front Physiol* **5**, 380, doi:10.3389/fphys.2014.00380 (2014).
20 A novel gene containing a trinucleotide repeat that is expanded and unstable on Huntington's disease chromosomes. The Huntington's Disease Collaborative Research Group. *Cell* **72**, 971-983, doi:10.1016/0092-8674(93)90585-e (1993).
21 Neueder, A., Dumas, A. A., Benjamin, A. C. & Bates, G. P. Regulatory mechanisms of incomplete huntingtin mRNA splicing. *Nat Commun* **9**, 3955, doi:10.1038/s41467-018-06281-3 (2018).

22 Ross, C. A. & Tabrizi, S. J. Huntington's disease: from molecular pathogenesis to clinical treatment. *Lancet Neurol* **10**, 83-98, doi:10.1016/S1474-4422(10)70245-3 (2011).
23 Saudou, F., Finkbeiner, S., Devys, D. & Greenberg, M. E. Huntingtin acts in the nucleus to induce apoptosis but death does not correlate with the formation of intranuclear inclusions. *Cell* **95**, 55-66, doi:10.1016/s0092-8674(00)81782-1 (1998).
24 Ghosh, R. *et al.* Expression of mutant exon 1 huntingtin fragments in human neural stem cells and neurons causes inclusion formation and mitochondrial dysfunction. *FASEB J* **34**, 8139-8154, doi:10.1096/fj.201902277RR (2020).
25 Bozzi, M. & Sciandra, F. Molecular Mechanisms Underlying Muscle Wasting in Huntington's Disease. *Int J Mol Sci* **21**, doi:10.3390/ijms21218314 (2020).
26 Ciammola, A. *et al.* Increased apoptosis, Huntingtin inclusions and altered differentiation in muscle cell cultures from Huntington's disease subjects. *Cell Death Differ* **13**, 2068-2078, doi:10.1038/sj.cdd.4401967 (2006).
27 Ciammola, A. *et al.* Low anaerobic threshold and increased skeletal muscle lactate production in subjects with Huntington's disease. *Mov Disord* **26**, 130-137, doi:10.1002/mds.23258 (2011).
28 Kojer, K. *et al.* Huntingtin Aggregates and Mitochondrial Pathology in Skeletal Muscle but not Heart of Late-Stage R6/2 Mice. *J Huntingtons Dis* **8**, 145-159, doi:10.3233/JHD-180324 (2019).
29 Lodi, R. *et al.* Abnormal in vivo skeletal muscle energy metabolism in Huntington's disease and dentatorubropallidoluysian atrophy. *Ann Neurol* **48**, 72-76 (2000).
30 Orth, M., Cooper, J. M., Bates, G. P. & Schapira, A. H. Inclusion formation in Huntington's disease R6/2 mouse muscle cultures. *J Neurochem* **87**, 1-6, doi:10.1046/j.1471-4159.2003.02009.x (2003).
31 Russell, O. M. *et al.* Preferential amplification of a human mitochondrial DNA deletion in vitro and in vivo. *Sci Rep* **8**, 1799, doi:10.1038/s41598-018-20064-2 (2018).
32 Lutz, A. K. *et al.* Autism-associated SHANK3 mutations impair maturation of neuromuscular junctions and striated muscles. *Sci Transl Med* **12**, doi:10.1126/scitranslmed.aaz3267 (2020).
33 Harrington, D. L. *et al.* Network topology and functional connectivity disturbances precede the onset of Huntington's disease. *Brain* **138**, 2332-2346, doi:10.1093/brain/awv145 (2015).
34 Poudel, G. R. *et al.* Abnormal synchrony of resting state networks in premanifest and symptomatic Huntington disease: the IMAGE-HD study. *J Psychiatry Neurosci* **39**, 87-96, doi:10.1503/jpn.120226 (2014).
35 Poudel, G. R., Harding, I. H., Egan, G. F. & Georgiou-Karistianis, N. Network spread determines severity of degeneration and disconnection in Huntington's disease. *Hum Brain Mapp* **40**, 4192-4201, doi:10.1002/hbm.24695 (2019).
36 Tabrizi, S. J. *et al.* Biological and clinical changes in premanifest and early stage Huntington's disease in the TRACK-HD study: the 12-month longitudinal analysis. *Lancet Neurol* **10**, 31-42, doi:10.1016/S1474-4422(10)70276-3 (2011).
37 Tabrizi, S. J. *et al.* Predictors of phenotypic progression and disease onset in premanifest and early-stage Huntington's disease in the TRACK-HD study:

analysis of 36-month observational data. *Lancet Neurol* **12**, 637-649, doi:10.1016/S1474-4422(13)70088-7 (2013).

38 van den Heuvel, M. P. & Sporns, O. Rich-club organization of the human connectome. *J Neurosci* **31**, 15775-15786, doi:10.1523/JNEUROSCI.3539-11.2011 (2011).

39 Rienecker, K. D. A., Poston, R. G. & Saha, R. N. Merits and Limitations of Studying Neuronal Depolarization-Dependent Processes Using Elevated External Potassium. *ASN Neuro* **12**, 1759091420974807, doi:10.1177/1759091420974807 (2020).

40 Reddy, P. H. Increased mitochondrial fission and neuronal dysfunction in Huntington's disease: implications for molecular inhibitors of excessive mitochondrial fission. *Drug Discov Today* **19**, 951-955, doi:10.1016/j.drudis.2014.03.020 (2014).

41 Uhlen, M. *et al.* Proteomics. Tissue-based map of the human proteome. *Science* **347**, 1260419, doi:10.1126/science.1260419 (2015).

42 Brettschneider, J., Del Tredici, K., Lee, V. M. & Trojanowski, J. Q. Spreading of pathology in neurodegenerative diseases: a focus on human studies. *Nat Rev Neurosci* **16**, 109-120, doi:10.1038/nrn3887 (2015).

43 McColgan, P. *et al.* Selective vulnerability of Rich Club brain regions is an organizational principle of structural connectivity loss in Huntington's disease. *Brain* **138**, 3327-3344, doi:10.1093/brain/awv259 (2015).

44 Raj, A., Kuceyeski, A. & Weiner, M. A network diffusion model of disease progression in dementia. *Neuron* **73**, 1204-1215, doi:10.1016/j.neuron.2011.12.040 (2012).

45 Zhou, J., Gennatas, E. D., Kramer, J. H., Miller, B. L. & Seeley, W. W. Predicting regional neurodegeneration from the healthy brain functional connectome. *Neuron* **73**, 1216-1227, doi:10.1016/j.neuron.2012.03.004 (2012).

46 Cartaud, A., Stetzkowski-Marden, F., Maoui, A. & Cartaud, J. Agrin triggers the clustering of raft-associated acetylcholine receptors through actin cytoskeleton reorganization. *Biol Cell* **103**, 287-301, doi:10.1042/BC20110018 (2011).

47 Burke, K. A., Yates, E. A. & Legleiter, J. Biophysical insights into how surfaces, including lipid membranes, modulate protein aggregation related to neurodegeneration. *Front Neurol* **4**, 17, doi:10.3389/fneur.2013.00017 (2013).

48 Gao, X. *et al.* Cholesterol Modifies Huntingtin Binding to, Disruption of, and Aggregation on Lipid Membranes. *Biochemistry* **55**, 92-102, doi:10.1021/acs.biochem.5b00900 (2016).

49 Suopanki, J. *et al.* Interaction of huntingtin fragments with brain membranes--clues to early dysfunction in Huntington's disease. *J Neurochem* **96**, 870-884, doi:10.1111/j.1471-4159.2005.03620.x (2006).

50 Trevino, R. S. *et al.* Fibrillar structure and charge determine the interaction of polyglutamine protein aggregates with the cell surface. *J Biol Chem* **287**, 29722-29728, doi:10.1074/jbc.M112.372474 (2012).

51 Atwal, R. S. *et al.* Huntingtin has a membrane association signal that can modulate huntingtin aggregation, nuclear entry and toxicity. *Hum Mol Genet* **16**, 2600-2615, doi:10.1093/hmg/ddm217 (2007).

52 Harjes, P. & Wanker, E. E. The hunt for huntingtin function: interaction partners tell many different stories. *Trends Biochem Sci* **28**, 425-433, doi:10.1016/S0968-0004(03)00168-3 (2003).

53 Reddy, P. H. & Shirendeb, U. P. Mutant huntingtin, abnormal mitochondrial dynamics, defective axonal transport of mitochondria, and selective synaptic degeneration in Huntington's disease. *Biochim Biophys Acta* **1822**, 101-110, doi:10.1016/j.bbadis.2011.10.016 (2012).

54 Shirendeb, U. *et al.* Abnormal mitochondrial dynamics, mitochondrial loss and mutant huntingtin oligomers in Huntington's disease: implications for selective neuronal damage. *Hum Mol Genet* **20**, 1438-1455, doi:10.1093/hmg/ddr024 (2011).

55 Miranda, D. R. *et al.* Progressive Cl- channel defects reveal disrupted skeletal muscle maturation in R6/2 Huntington's mice. *J Gen Physiol* **149**, 55-74, doi:10.1085/jgp.201611603 (2017).

56 Waters, C. W., Varuzhanyan, G., Talmadge, R. J. & Voss, A. A. Huntington disease skeletal muscle is hyperexcitable owing to chloride and potassium channel dysfunction. *Proc Natl Acad Sci U S A* **110**, 9160-9165, doi:10.1073/pnas.1220068110 (2013).

57 Khedraki, A. *et al.* Depressed Synaptic Transmission and Reduced Vesicle Release Sites in Huntington's Disease Neuromuscular Junctions. *J Neurosci* **37**, 8077-8091, doi:10.1523/JNEUROSCI.0313-17.2017 (2017).

Figure 1

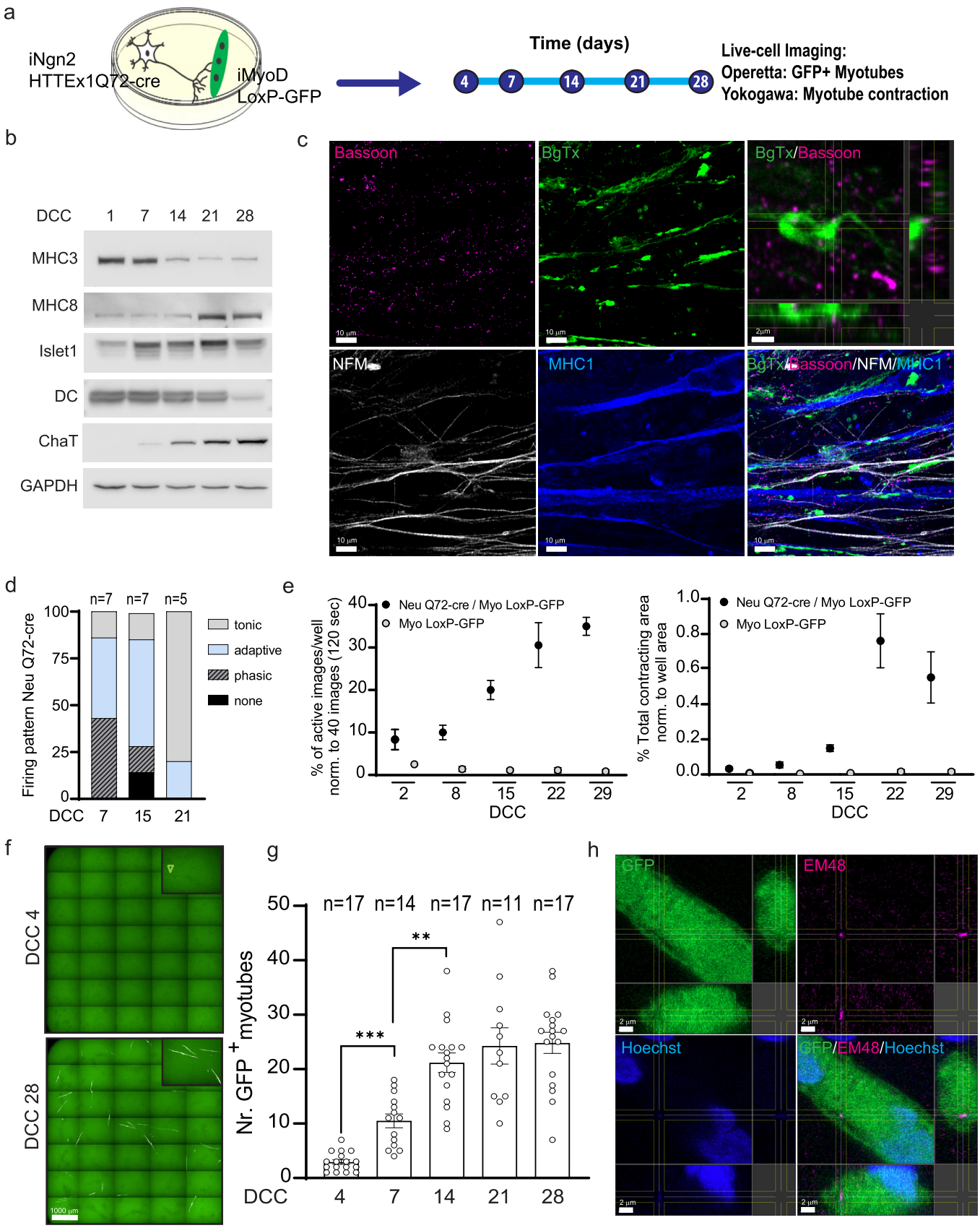

Figure 2

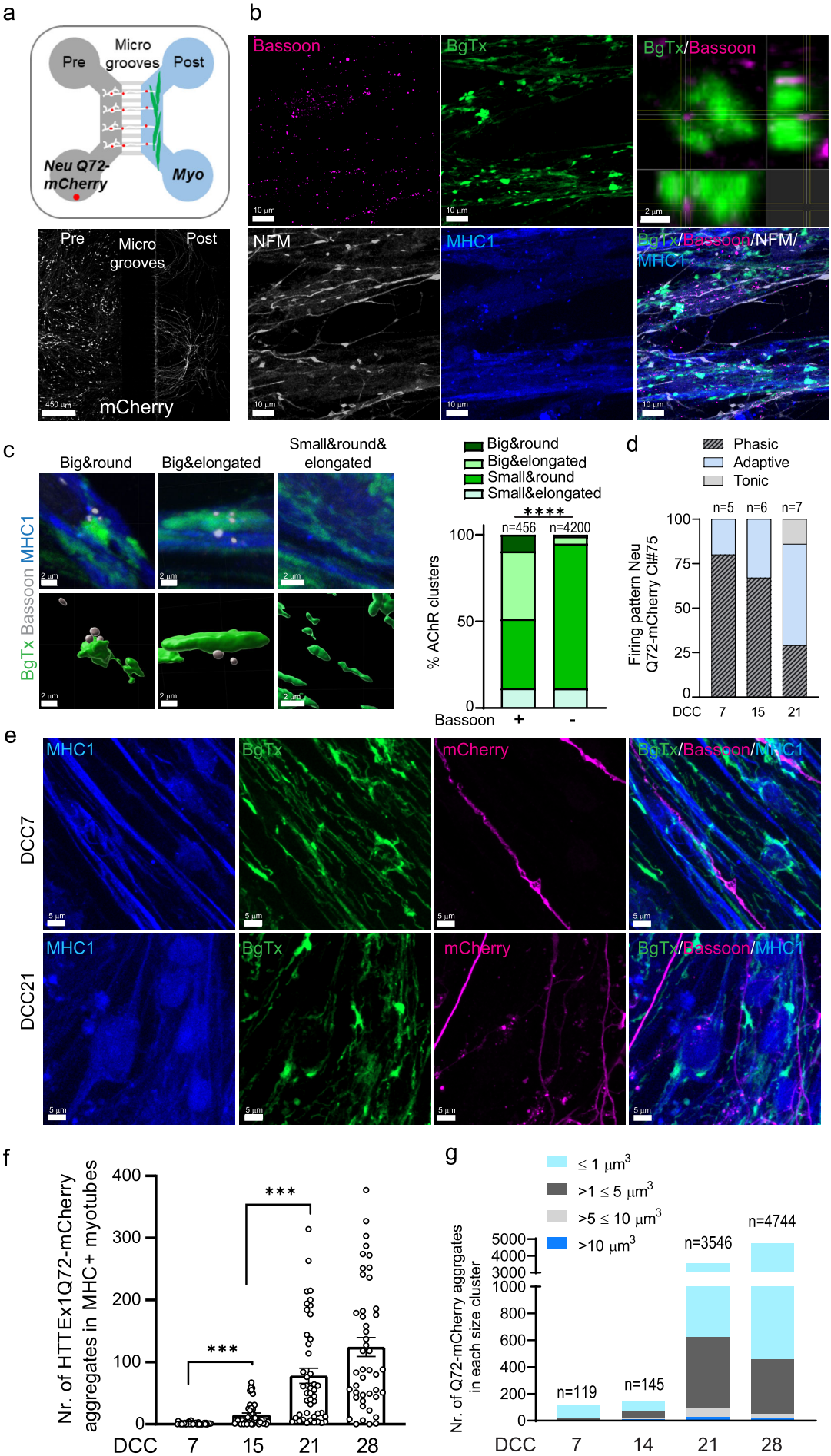

Figure 3

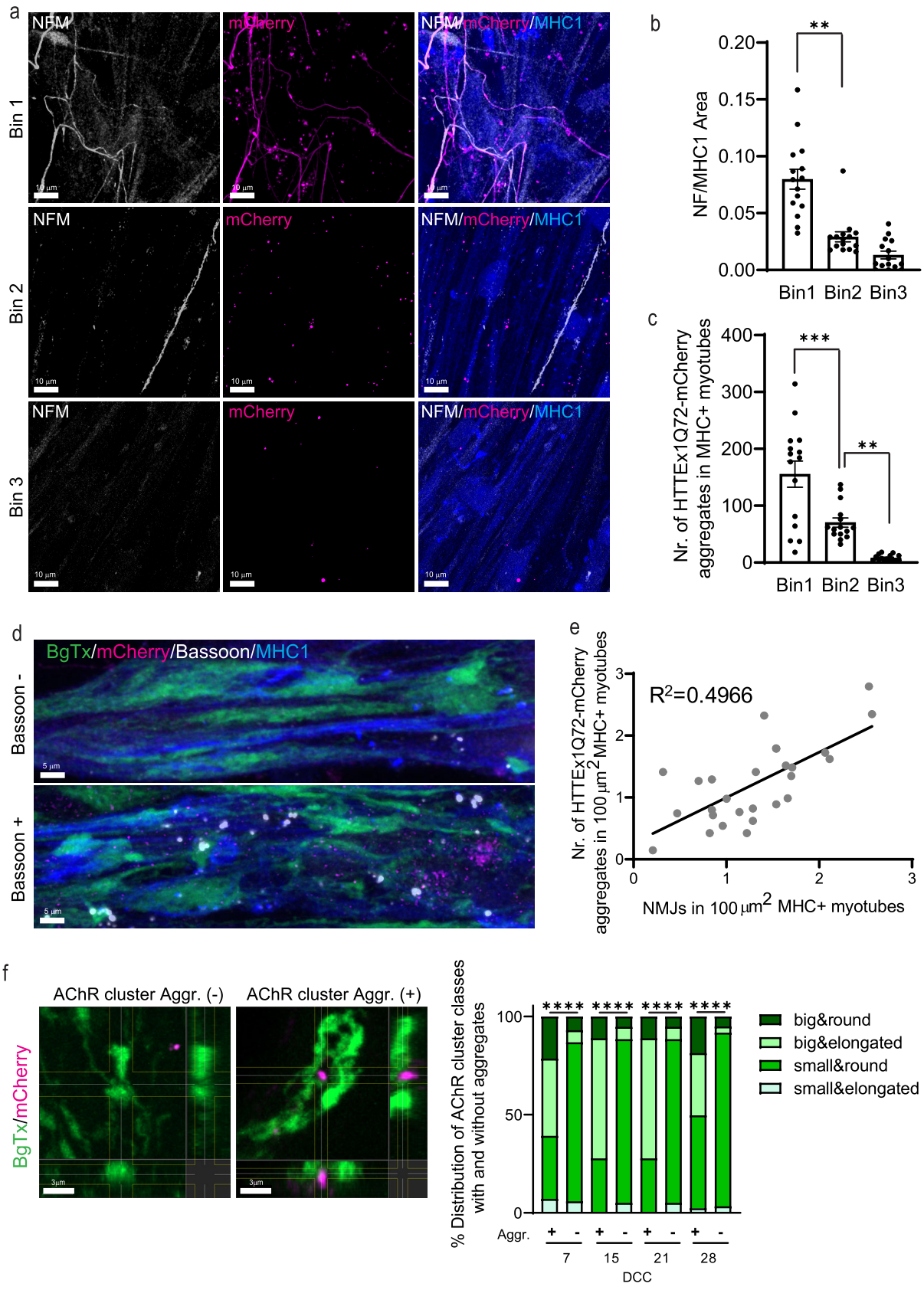

Figure 4

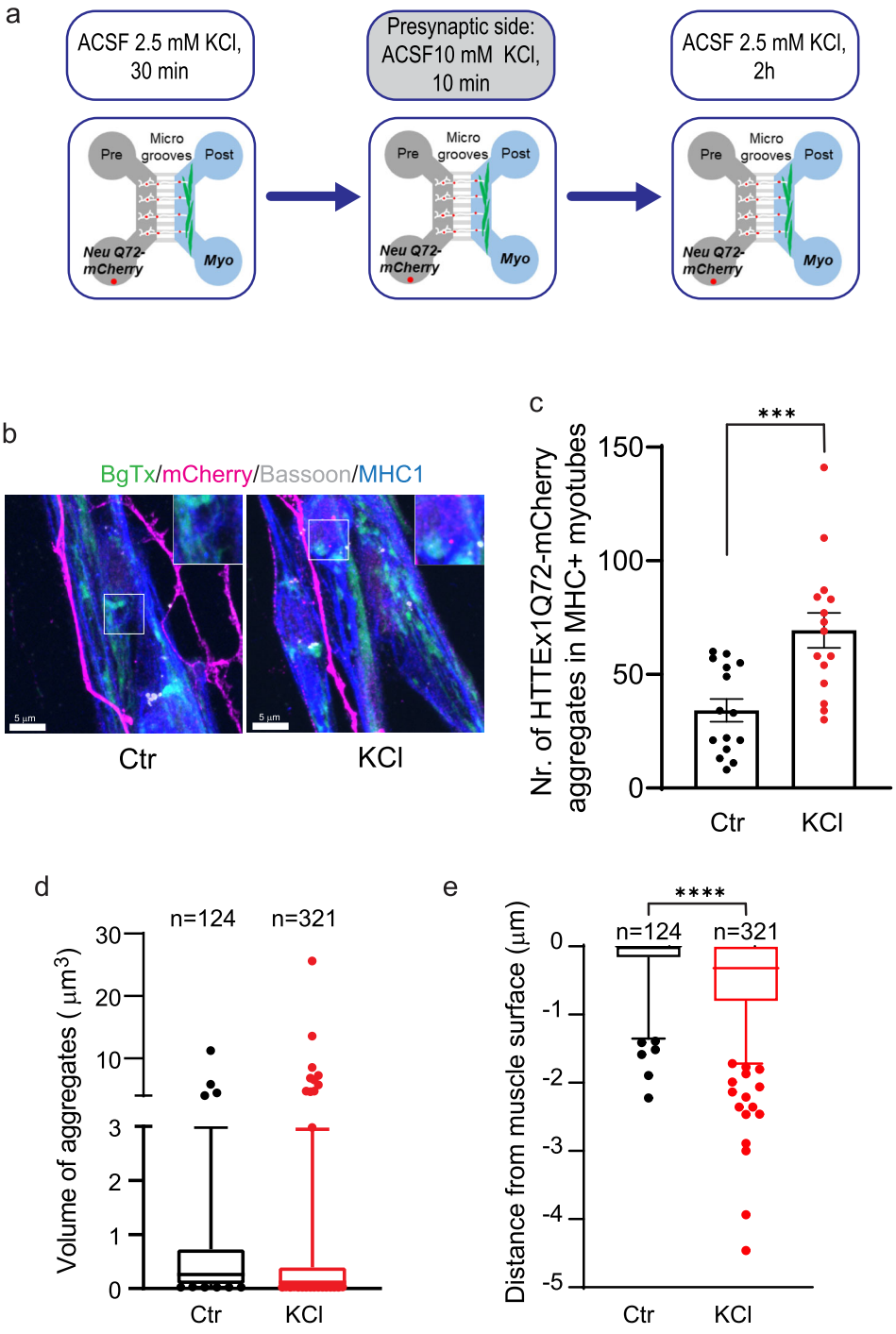

Figure 5

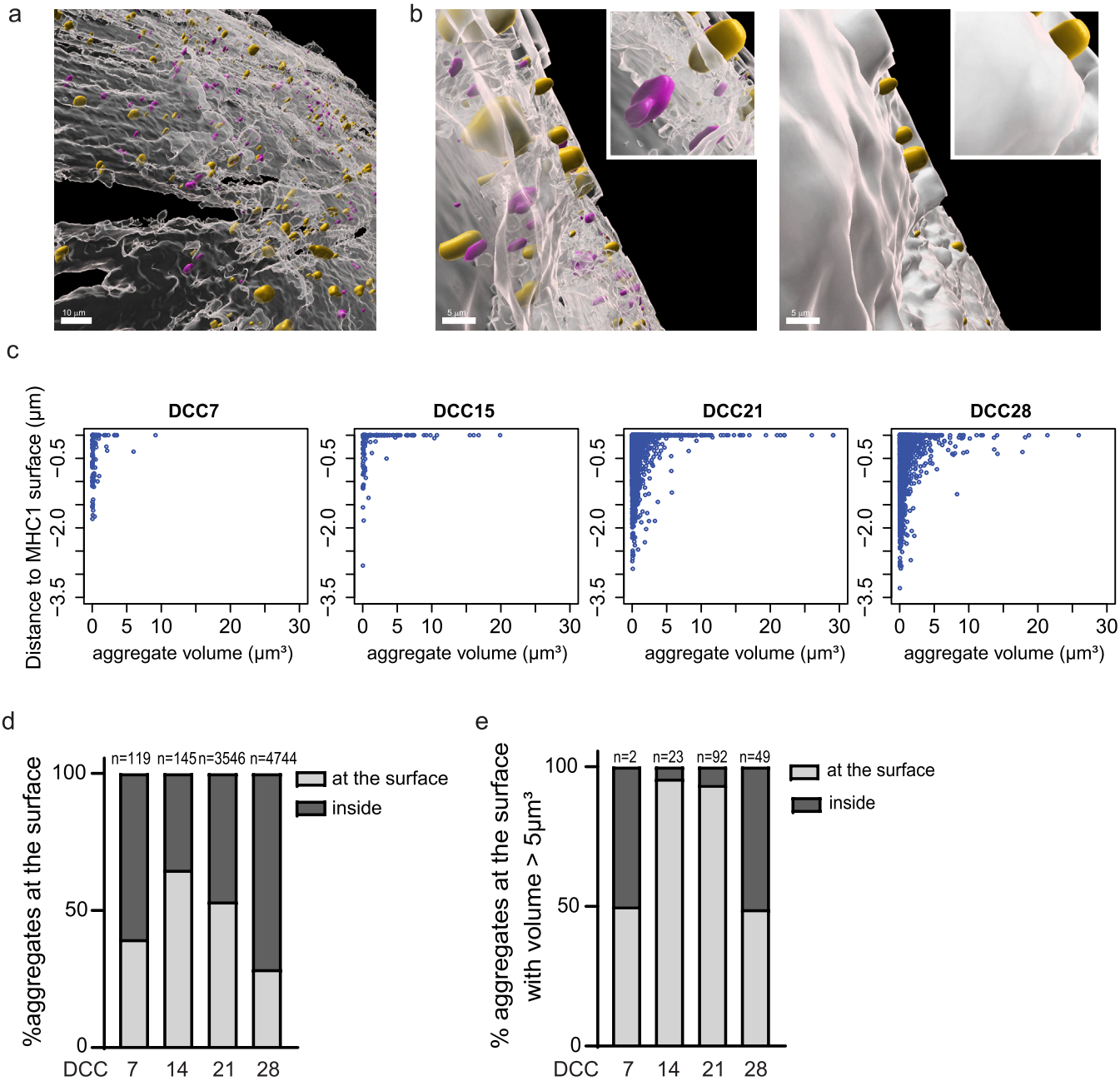

Figure 6

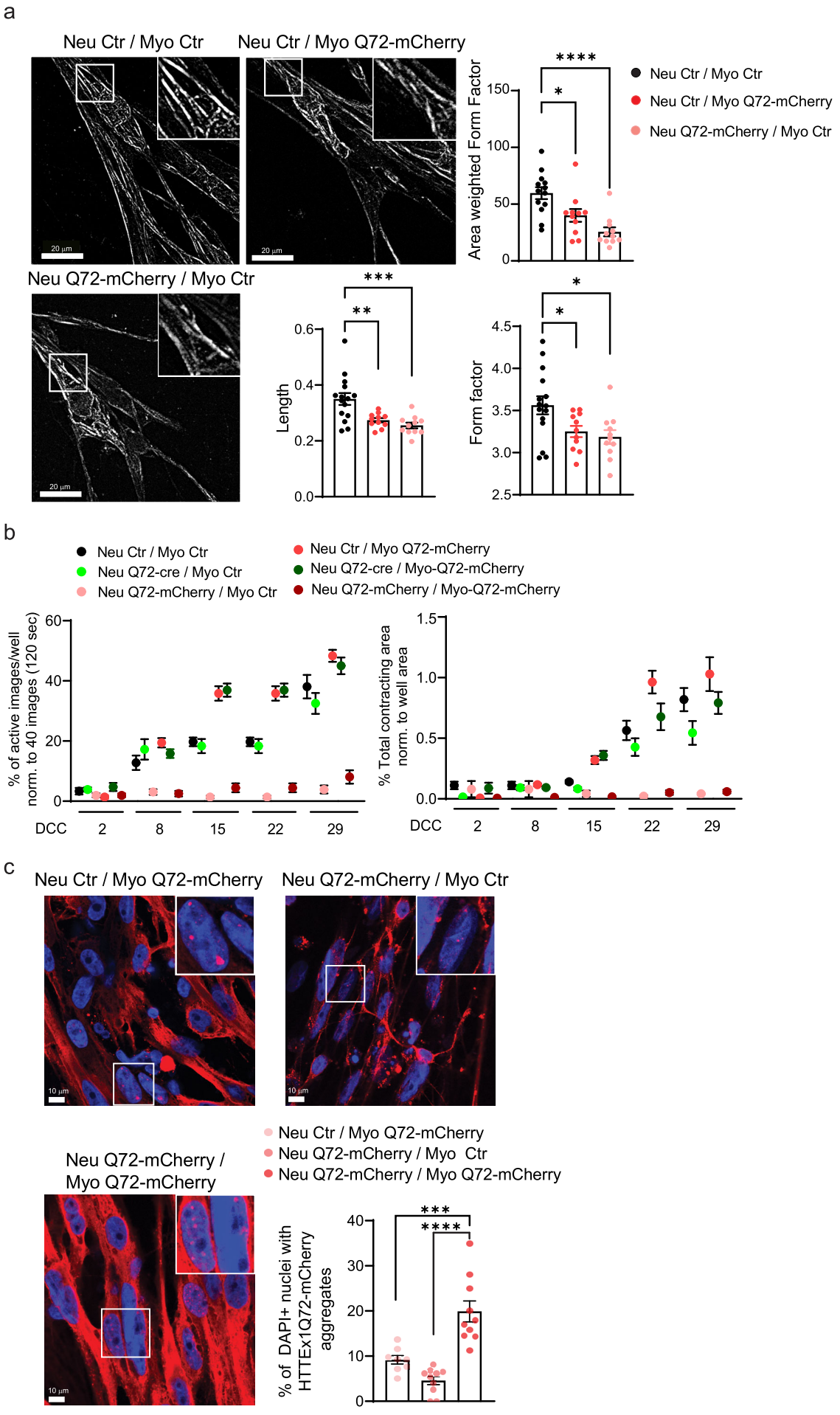

Figure 7